

Aerial Damage Survey of the 2013 El Reno Tornado Combined with Mobile Radar Data

ROGER M. WAKIMOTO,* NOLAN T. ATKINS,⁺ KELLY M. BUTLER,⁺# HOWARD B. BLUESTEIN,[@]
KYLE THIEM,[@] JEFFREY C. SNYDER,[&] JANA HOUSER,[#] KAREN KOSIBA,** AND JOSHUA WURMAN**

* *Department of Atmospheric and Oceanic Science, University of Colorado Boulder, Boulder, Colorado*

⁺ *Department of Atmospheric Sciences, Lyndon State College, Lyndonville, Vermont*

[#] *Department of Geography, Ohio University, Athens, Ohio*

[@] *School of Meteorology, University of Oklahoma, Norman, Oklahoma*

[&] *Cooperative Institute for Mesoscale Meteorological Studies, University of Oklahoma, and
NOAA/OAR/National Severe Storms Laboratory, Norman, Oklahoma*

** *Center for Severe Weather Research, Boulder, Colorado*

(Manuscript received 16 October 2015, in final form 28 January 2016)

ABSTRACT

A detailed damage survey of the El Reno, Oklahoma, tornado of 31 May 2013 combined with rapid-scanning data recorded from two mobile radars is presented. One of the radars was equipped with polarimetric capability. The relationship between several suction vortices visually identified in pictures with the high-resolution Doppler velocity data and swath marks in fields is discussed. The suction vortices were associated with small shear features in Doppler velocity and a partial ringlike feature of high spectral width. For the first time, a suction vortex that created a swath mark in a field was visually identified in photographs and high-definition video while the rotational couplet was tracked by radar. A dual-Doppler wind synthesis of the tornadic circulation at low levels near the location of several storm chaser fatalities resolved ground-relative wind speeds in excess of 90 m s^{-1} , greater than the minimum speed for EF5 damage. The vertical vorticity analysis revealed a rapid transition from a single tornadic vortex centered on the weak-echo hole (WEH) to suction vortices surrounding the WEH and collocated with the ring of enhanced radar reflectivities. Several bands/zones of enhanced convergence were resolved in the wind syntheses. One of the bands was associated with an internal or secondary rear-flank gust front. An inner band of convergence appeared to be a result of the positive bias in tornado-relative radial velocity owing to centrifuging of large lofted debris swirling within the tornado. An outer band of convergence formed at the northern edge of a region of strong inflow that was lofting small debris and dust into the storm.

1. Introduction

Detailed damage surveys in the aftermath of tornadoes have increased our understanding of both the intensity and the low-level structure of these circulations (e.g., Fujita 1981). A number of studies, however, have raised caution regarding estimates of the intensity based on observed damage since it requires knowledge of the structural responses to wind (e.g., Marshall 2002; Doswell

et al. 2009; Edwards et al. 2013). In addition, damage surveys in rural areas largely devoid of buildings are challenging owing to the low number of damage indicators (e.g., Doswell and Burgess 1988; Doswell et al. 2009; Edwards et al. 2013) although downed trees and scoured vegetation have often provided useful information to estimate the tornado's intensity and defining the near-ground wind field (e.g., Fujita 1989, 1992; Bech et al. 2009; Beck and Dotzek 2010; Karstens et al. 2013). In recent years, increased understanding of the damage caused by tornadoes has been achieved with the inclusion of low-level scans of high-resolution mobile radar data (e.g., Burgess et al. 2002; Wurman and Alexander 2005; Bodine et al. 2013; Snyder and Bluestein 2014; Wurman et al. 2014; Kurdzo et al. 2015).

Although tornadoes are often associated with a single vortex, they can exist as multiple suction/subvortices

 Denotes Open Access content.

Corresponding author address: Roger M. Wakimoto, National Science Foundation, 4201 Wilson Blvd, Rm. 705, Arlington, VA 22230.

E-mail: wakimotoroger@gmail.com

DOI: 10.1175/MWR-D-15-0367.1

© 2016 American Meteorological Society

(these features will be referred to as “suction vortices” herein) revolving around a central axis of rotation. Suction vortices associated with tornadoes have been extensively documented in photographs, movies, and video (e.g., Fujita 1981), damage surveys (e.g., Fujita et al. 1970, 1976; Fujita 1981), and radar studies (e.g., Bluestein et al. 1997, 2015; Wurman 2002; Wurman and Kosiba 2013; Wurman et al. 2014). There has been no study in the refereed literature, however, that combines photogrammetric analyses of suction vortices, suction swaths documented in an aerial damage survey, and high-resolution radar data owing to the difficulty of obtaining contemporaneous measurements.

On 31 May 2013, a large tornado produced a swath of damage ~26 km long near El Reno, Oklahoma. Fortunately, the tornado remained mostly over open terrain and damaged few structures; however, several storm chasers were killed by the tornado and it also injured passengers in a Weather Channel vehicle as they attempted to outrun the vortex (Wurman et al. 2014). A multiscale overview of the tornadic supercell has been discussed by Bluestein et al. (2015). Wurman et al. (2014) have analyzed single-Doppler velocity data collected by mobile radars and described this event as a tornado/multiple vortex mesocyclone (Wurman and Kosiba 2013). Many of the vortices moved in trochoidal-like paths, making it challenging at times to differentiate the tornado from suction vortices.

This study presents a detailed analysis of the damage track left behind by the tornado based on a ground and comprehensive aerial survey. This analysis is augmented by the availability of high-resolution data collected from two mobile, rapid-scanning, 3-cm (X band) radars. One of the radars was equipped with polarimetric capability. Dual-Doppler wind syntheses at low levels were created during a time when the tornado was near its maximum intensity. The combination of the wind synthesis with polarimetric data provided additional insight into the swirling debris field produced by the tornado. A series of photographs and high-resolution video were recorded at two locations near the tornado track. This visual documentation captured the characteristics of the main funnel and several suction vortices. There have been a number of prior studies that have included aspects of the El Reno dataset (e.g., Wurman and Alexander 2005; Bluestein et al. 2007; Wakimoto et al. 2011; Bodine et al. 2013; Wurman et al. 2013, 2014; Atkins et al. 2014; Houser et al. 2015, 2016, manuscript submitted to *Mon. Wea. Rev.*; Kurdzo et al. 2015). However, the combination of a detailed damage survey, photogrammetry, and mobile radar with rapid-scan capability used in the present study is unique.

Descriptions of the Rapid-Scan Doppler on Wheels (RSDOW) and Rapid Scan X-band Polarimetric

Doppler Radar (RaXPoL) as well as an overview of the damage survey are presented in section 2. Section 3 describes the results of a merger of the damage survey and mobile radar data with the visual features of the tornado based on a photogrammetric analysis of high-resolution video and pictures. A detailed analysis of an intense suction vortex is also discussed. A dual-Doppler wind synthesis at low levels using the two rapidly scanning radars is shown in section 4 and a discussion and summary is presented in section 5.

2. RSDOW, RaXPOL, and the overview of the damage survey

While mobile radars have been deftly used to collect high-resolution data on tornadoes for a number of years, the requirement for rapidly scanning systems has been clearly established (e.g., Keeler and Passarelli 1990; Bluestein et al. 2001). Data from two rapidly scanning radars that were deployed on the El Reno storm are used in the present study. RSDOW (Wurman and Randall 2001; Wurman et al. 2013, 2014) transmits six simultaneous, vertically stacked beams to provide rapid volumetric updates. RSDOW (also referred to as DOW8) uses a slotted waveguide array antenna and a multichannel receiver. The antenna scans mechanically in azimuth producing 360° volumetric information every ~7 s. The half-power beamwidth is ~0.9° and each elevation angle is separated by 1° (lowest elevation angle is 0.5°). The range resolution (the distance between data samples in a radar beam) was 50 m. The interested reader is referred to Wurman and Randall (2001) for additional information.

RaXPoL (Pazmany et al. 2013) is equipped with an antenna on a pedestal that rotates at a maximum of 180° s⁻¹ and a half-power beamwidth that is 1°, although the dwell time required to collect samples for moment calculations typically results in an effective beamwidth of ~1.4° owing to beam smearing.¹ The range resolution was 75 m, oversampled such that range gate spacing was 45 m for data collection before 2306 UTC. After 2306 UTC, the resolution and gate spacing were 30 and 15 m, respectively. Frequency diversity (e.g., Hildebrand and Moore 1990) is used to increase the number of independent samples needed to calculate the radar parameters while in rapid-scan mode. The interested reader is referred to Pazmany et al. (2013) for additional information on RaXPoL.

¹Pazmany et al. (2013) have devised a “strobe technique” that can remove the beam smearing but it was not used during data collection on 31 May 2013.

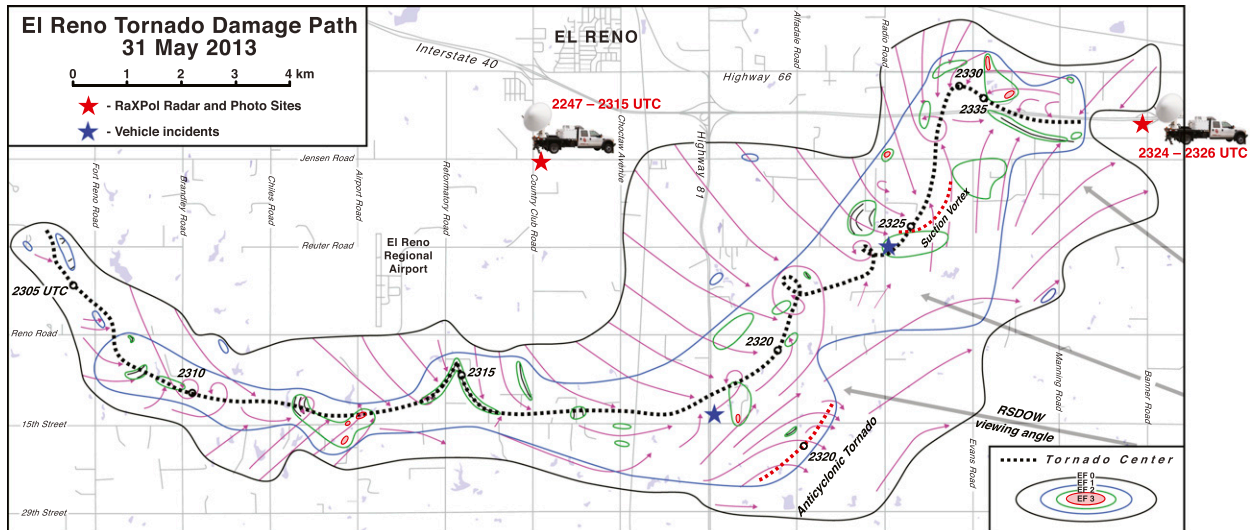


FIG. 1. Damage map of the El Reno, OK, tornado on 31 May 2013. Black, blue, green, and red contours denote the EF0, -1, -2, and -3 damage intensity isopleths, respectively. Black dashed line is the center of the tornado. The two red dashed lines denote the location of an anticyclonic tornado and cyclonic suction vortex. Magenta lines represent the approximate flow as depicted in the damage based on fallen trees, building debris, and streaks in the vegetation based on a detailed aerial survey. Red stars represent two deployment locations of the RaXPoL mobile Doppler radar (shown by an icon of the truck). Deployment times are also indicated. Photographs and high-definition video of the tornado were taken at both sites. Blue stars represent the locations where the car driven by The Weather Channel crew (near Highway 81 and 15th street) and a storm chasers' vehicle (near Radio Road and Reuter Road) were found. Gray arrows represent the viewing angles from the RSDOW site.

The El Reno tornado occurred in a rural area with few structures and people exposed to the intense winds. The absence of structures that were damaged led to a lengthy debate regarding the final National Weather Service (NWS) enhanced Fujita (EF) rating of 3 (EF3). Doppler velocities measured by mobile radars suggested much higher wind speeds located above the surface ($>130 \text{ m s}^{-1}$) exceeding those associated with an EF5 rating (Snyder and Bluestein 2014; Wurman et al. 2014; Bluestein et al. 2015). Ground damage surveys were conducted on 1 and 3 June and a comprehensive aerial survey was performed on 4 June. The latter was accomplished using a Cessna 172 flying at 300 and 1200 m AGL (above ground level). A total of 1249 aerial photographs were taken along the tornado track. The NWS EF kit (LaDue and Mahoney 2006) was used to estimate EF damage intensity to structures. In addition, the direction of tree fall, scattered debris, and bales of hay were plotted on to topographic maps. The damage analysis based on the aerial survey was combined with the ground survey data collected by Marshall et al. (2014) and D. Burgess (2014, personal communication) to produce the final damage mapping. Most of the damage indicators determined from the aerial survey agreed with the estimates based on the ground survey. In the few instances where the damage indicators differed, the ground-based estimate was chosen as the final assigned EF value. The isopleths of the EF damage are

shown in Fig. 1. The contoured field shown differs from the map presented by Marshall et al. (2014, see their Fig. 10). These differences are almost exclusively a result of the numerous damage indicators identified in the open fields (e.g., swath marks and downed trees in the middle of a field). These indicators would have been difficult to identify and assess from the ground survey which was largely confined to roads and driveways.

The track of the tornado is shown by the dashed, black line and was determined from both radar locations of the velocity couplet and the aerial damage survey and is consistent with the results presented by Wurman et al. (2014). The two RaXPoL deployment sites used in the present study are indicated by the red stars in Fig. 1. One location was near the intersection of Jensen and Country Club Roads (referred to as “site 1” herein) while the other location was near the intersection of Banner Road and Interstate 40 (referred to as “site 2” herein). The El Reno tornado was located 4–9 and 4–5 km from RaXPoL at sites 1 and 2, respectively. RSDOW was located to the east of the tornado (shown by the viewing angles in Fig. 1) and ranged from 10 to 16 km from the center of the tornado track. Fortunately, the deployments of the two radars resulted in data collection over most of the life cycle of the El Reno tornado. RaXPoL collected data from the beginning of the damage track to just east of Reformatory Road (southeast of the El Reno Regional

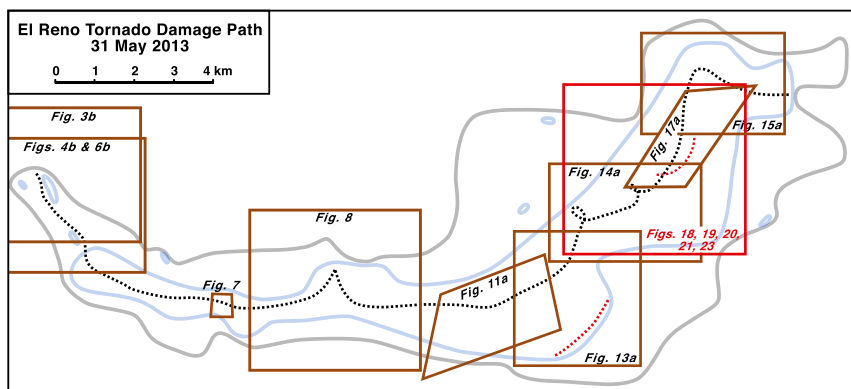


FIG. 2. Damage map of the El Reno tornado. The tornado track is shown by the black dashed line. The two red dashed lines denote the location of an anticyclonic tornado and cyclonic suction vortex. The EF0 and -1 isopleths are shown by the gray and light blue lines scale, respectively. Brown and red boxes denote regions that are enlarged in subsequent figures. Each box is labeled with a figure number.

Airport) while it was positioned at site 1. RSDOW collected data on the tornado from approximately Choctaw Avenue until the circulation dissipated near Banner Road. Both radars were scanning the tornado when RaXPOL was repositioned at site 2. The subset of the data collected from site 2 of RaXPOL has been presented in Wakimoto et al. (2015). In addition, RaXPOL and RSDOW collected low-level data that could be combined into a dual-Doppler wind synthesis for several consecutive volumes when the tornado was located near the intersection of Radio and Reuter Roads. These syntheses were created during the time that the tornado was intense, with recorded single-Doppler velocities ranging from 120 to 130 m s^{-1} (Marshall et al. 2014; Snyder and Bluestein 2014; Wurman et al. 2014). However, there was a lack of surface damage indicators in this region.

The approximate U-shaped pattern in the outline of the EF0 isopleth south of El Reno in Fig. 1 is consistent with the NWS survey (e.g., Wurman et al. 2014; Bluestein et al. 2015, see their Fig. 8). The first indication of tornado damage occurred west of the intersection of Fort Reno and Reuter Roads. The tornado initially moved southeastward and then east toward Highway 81. The tornado turned toward the northeast just before the highway and continued in that general heading as it approached Interstate 40. Subsequently, the El Reno tornado headed to the east before dissipating near Banner Road. The width of the EF0 damage is large, reaching ~ 7 km just east of Highway 81. This damage width, however, is not entirely attributable to the El Reno tornado. Indeed, a separate anticyclonic tornado [first noted by Wurman et al. (2014)] near the intersection of Alfadale Road and 15th Street was identified in

both the mobile radar data and the damage survey (Fig. 1), which contributed to the extension of the damage to the southeast. In addition, the southern periphery of the EF0 isopleth east of Highway 81 suggests damage associated with the rear-flank downdraft (e.g., Fujita 1992; Karstens et al. 2013; Wurman et al. 2014). A series of boxes are superimposed onto an outline of the damage track (Fig. 2). The regions enclosed by the boxes will be enlarged in subsequent figures in order to highlight various aspects of the damage and radar analysis collected on this event.

3. Damage survey combined with radar and visual documentation

The analysis of the El Reno tornado provided an opportunity to combine high-resolution mobile radar data with the damage survey. In addition, a series of photographs and high-resolution videos were taken at the same location as the radar deployment site. Elevation- and azimuth-angle grids were created using photogrammetric techniques and superimposed on each image. These grids correspond to the radar scanning angles since the photographer and radar were collocated. A description of the photogrammetry analysis used in the current study has been presented in Wakimoto et al. (2015).

a. Tornadogenesis and the tornadic debris signature

The approximate time of tornadogenesis (2303:14 UTC) is shown in Fig. 3. The wall cloud is visually apparent (Fig. 3a) with the north and south edges highlighted by the azimuthal angles that are also drawn on Fig. 3b. The wall cloud was ~ 1.32 km in diameter, and its

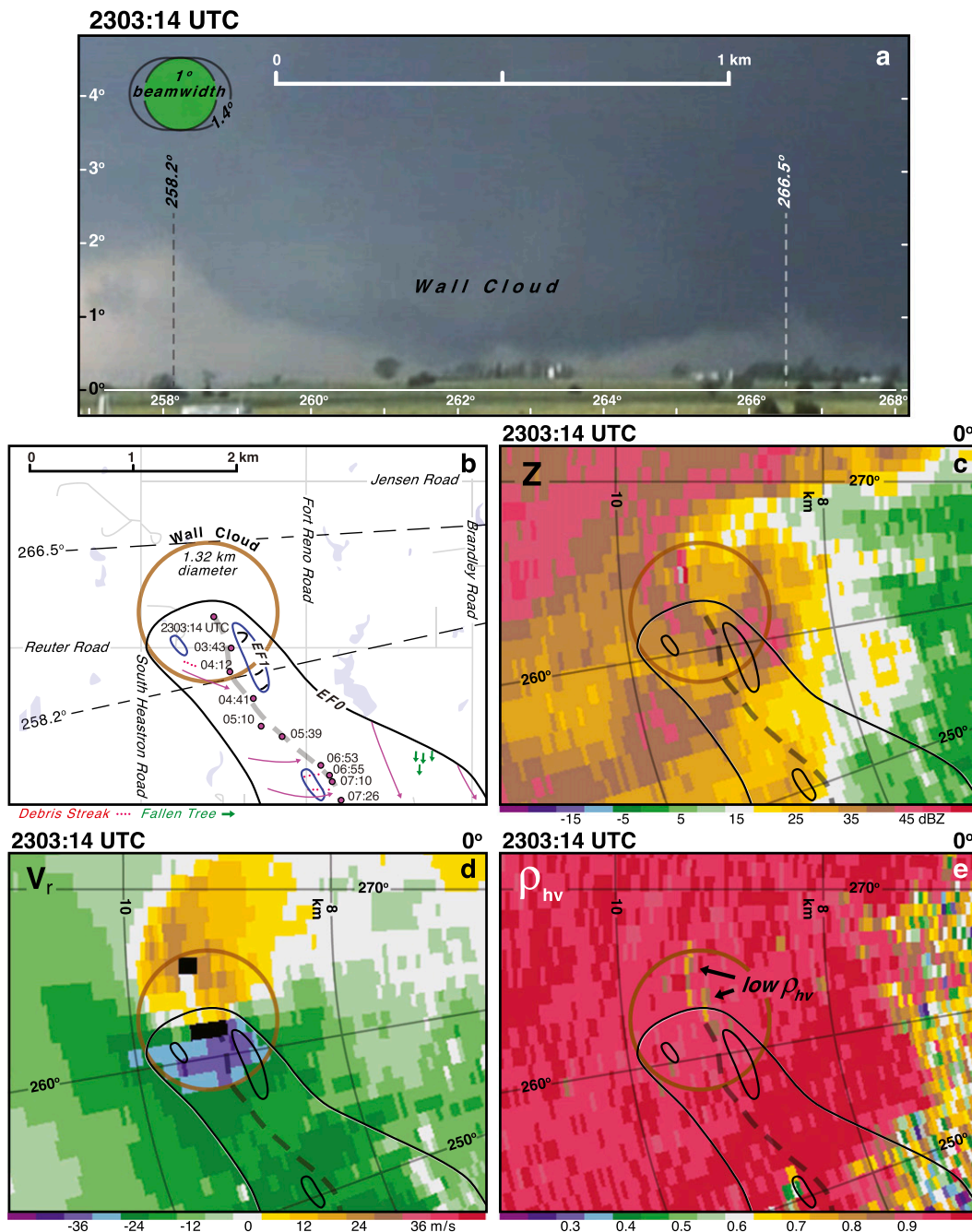


FIG. 3. (a) Photograph of the wall cloud at 2303:14 UTC at the beginning of the tornado track. Dashed lines represent the approximate north and south boundaries of the wall cloud. The length scale is valid at the center of the wall cloud. The green circle and the larger ellipse are the 1° beamwidth and the 1.4° effective beamwidth of RaXPoI, respectively. (b) Enlargement of the damage map at the beginning of the track. EF0 and -1 contours are drawn and the dashed gray line represents the center of the tornado track. Magenta circles represent the location of the rotational couplet with the times indicated. Dashed black lines are the azimuths shown in (a). Magenta lines represent the approximate flow as depicted in the damage based on fallen trees and building debris. (c) Radar reflectivity, (d) single-Doppler velocity, and (e) cross-correlation coefficient ρ_{hv} at 2303:14 UTC at 0°. The damage track is superimposed on (c),(d), and (e). The brown circle drawn in (b),(c),(d), and (e) is the approximate location of the wall cloud and is estimated to be 1.32 km in diameter. The black arrows in (e) denote the location of a few brown pixels of relatively low ρ_{hv} indicating lofted debris. Range and azimuth lines from RaXPoI are drawn in (c),(d), and (e). Area shown in (b) is depicted in Fig. 2.

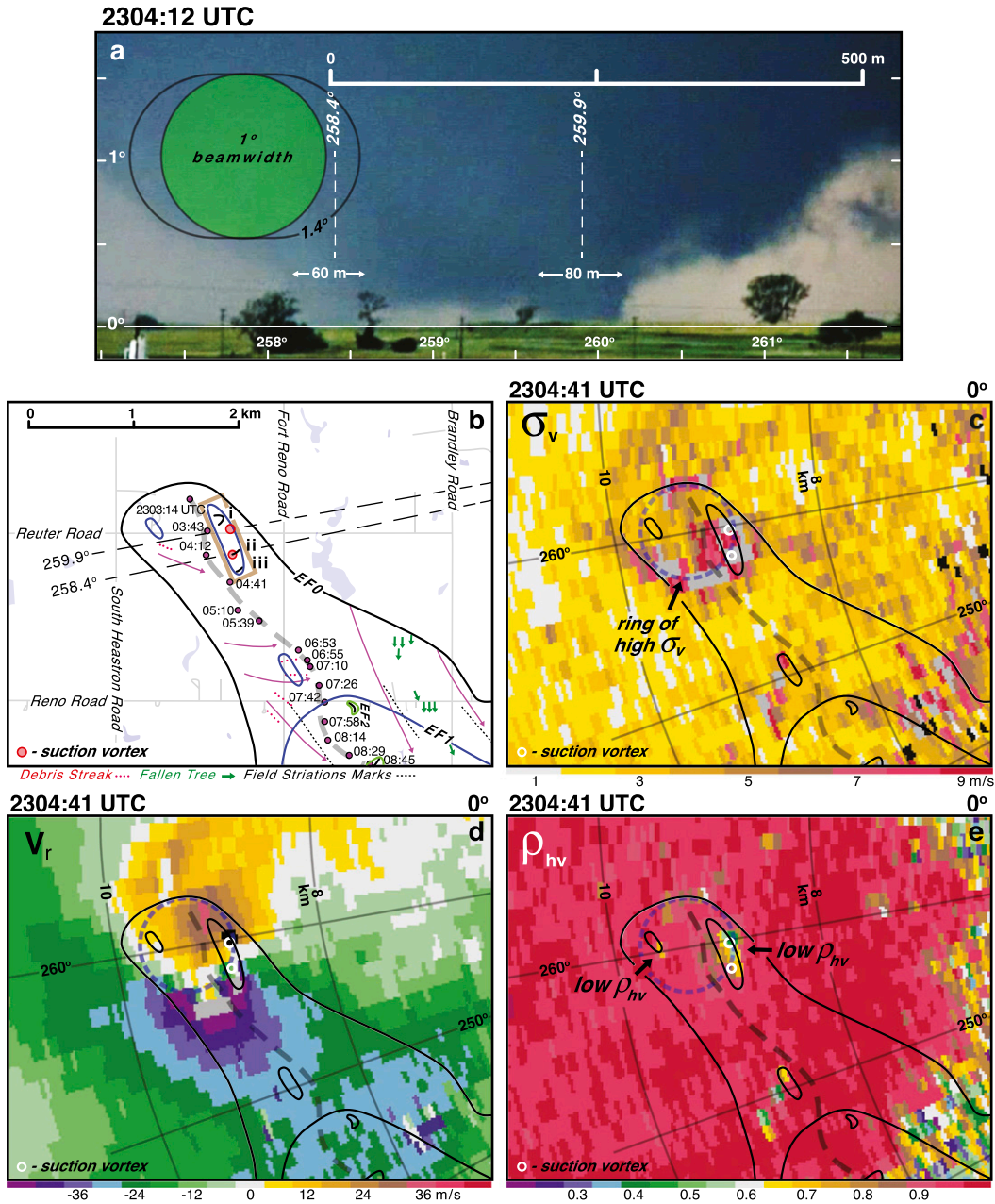


FIG. 4. (a) Photograph of two suction vortices at 2304:12 UTC. Dashed lines represent the azimuths to the center of the suction vortices. The green circle and the larger ellipse are the 1° beamwidth and the 1.4° effective beamwidth of RaXPoI, respectively. (b) Enlargement of the damage map at the beginning of the track. EF0 and -1 contours are drawn and the dashed gray line represents the center of the tornado track. Magenta circles represent the location of the rotational couplet with the times indicated. Brown box encompasses the suction swaths (labeled i, ii, and iii) and is enlarged in Fig. 5. Dashed black lines are the azimuths shown in (a). Magenta lines represent the approximate flow as depicted in the damage based on fallen trees, building debris, and field striation marks. (c) Spectral width σ_v , (d) single-Doppler velocity, and (e) cross-correlation coefficient ρ_{hv} at 2304:41 UTC at 0° . The damage track is superimposed on (c),(d), and (e). Red [in (b)] and white [in (c),(d), and (e)] circles represent the location and width of the funnels. The dashed circle drawn on (c),(d), and (e) denotes a ring of relatively high values of σ_v . Range and azimuth lines from RaXPoI are drawn on (c),(d), and (e). Area shown in (b) is depicted in Fig. 2.

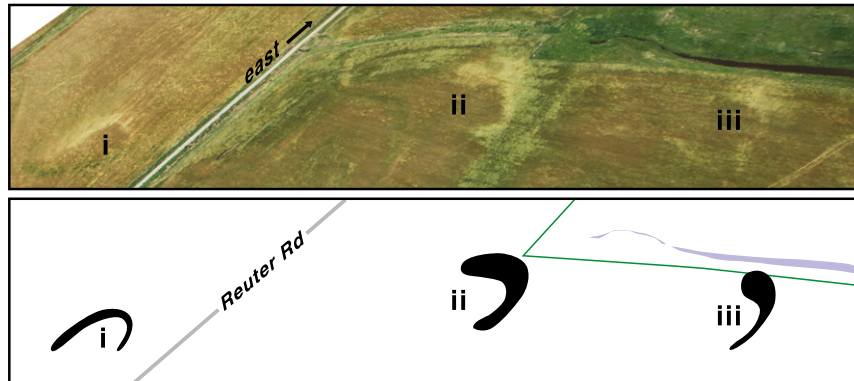


FIG. 5. Analysis of three suction swath marks. (top) An aerial photo looking east. (bottom) Highlighting the three marks. The region enlarged in this figure is shown in Fig. 4.

estimated position is shown in Fig. 3b by the brown circle. The radar reflectivity pattern suggests spiral bands converging on the location of the wall cloud (Fig. 3c), and a velocity couplet is apparent in Fig. 3d. The tornadic debris signature (TDS) is a radar signature that is typically accompanied by a strong rotational couplet, a local maximum in radar reflectivity, low differential reflectivity (Z_{DR}), and low cross-correlation coefficient (ρ_{hv}) (e.g., Kumjian and Ryzhkov 2008). The black arrows in Fig. 3e denote the location of a few pixels of relatively low values of ρ_{hv} (0.7–0.8), suggesting the presence of debris that has been lofted during the genesis stage. Figure 3e depicts the first systematic lowering of ρ_{hv} within the circulation. Subsequent times reveal lower values that also expand in areal extent. Wurman et al. (2014) also showed low ρ_{hv} with the early stages of the tornado but for a later time.

b. Suction vortex analysis early in the tornado's life cycle

A number of suction vortices were visible during the early stages of the tornado's life cycle. Two of these vortices are evident at 2304:12 UTC (Fig. 4a) and are separated by ~ 250 m. The southern and northern funnels are ~ 60 and 80 m in diameter, respectively, at low levels (~ 50 m AGL) and would be difficult to resolve based on the 1° beamwidth shown in Fig. 4a. The approximate locations and widths of the two suction vortices are shown by the red circles in Fig. 4b. These positions were chosen since they are collocated with small shear features on the Doppler velocity image (Fig. 4d), an area of low ρ_{hv} (Fig. 4e), and along a partial ringlike feature of high spectral width (Fig. 4c) denoted by the dashed circle. The latter suggests the presence of a region of enhanced turbulence where the rotation of the suction vortices around the tornado center is occurring [also noted by Wurman (2002)]. Moreover, the

location of the suction vortices corresponds to three suction swaths of damage that were identified in the aerial survey (labeled i, ii, and iii in Fig. 4b). Note that another debris signature (a few pixels of low ρ_{hv}) is located to the west of the suction swaths and is enclosed by the EF1 isopleth where a house was damaged (Fig. 4e).

The three crescent-shaped suction swaths are enclosed by the brown box (Fig. 4b) and are enlarged in Fig. 5. The southern suction vortex along the 258.4° azimuth appears to coincide with the location of the middle suction swath ii in Fig. 4b. The northern suction vortex is close to the location of the northern swath labeled i. The distance of RaXPOL from the tornado (9–10 km) is insufficient to unambiguously equate the appearance of suction vortices visible in the image (Fig. 4a) with the ground damage caused by suction swaths (Fig. 5) owing to the size of the beamwidth, but the analysis strongly suggests that a relationship exists. A single vortex was apparent at 2305:10 UTC (Fig. 6a) and it is encircled by a hooklike band of enhanced radar reflectivity (Fig. 6c). The rotational couplet and the TDS are centered within the damage path (Figs. 6d and 6e). The area of low ρ_{hv} collocated with the tornado track is different than the previous analysis and is consistent with the appearance of a single funnel in the photo. The narrow width of the funnel is apparent when examining the width of the area enclosed by the EF0 isopleth (Fig. 6b). A similar observation was noted by Atkins et al. (2014) for the 20 May 2013 Moore tornado. Previous research has not suggested a consistent relationship between the condensation funnel size relative to the damage path width (e.g., Golden and Purcell 1978; Bluestein et al. 1997; Wakimoto et al. 2003; Atkins et al. 2012, 2014).

c. Scouring marks and a cusp in the tornado track

Information regarding the tornado's location and kinematic features of the low-level wind field were determined in several areas devoid of structures. An

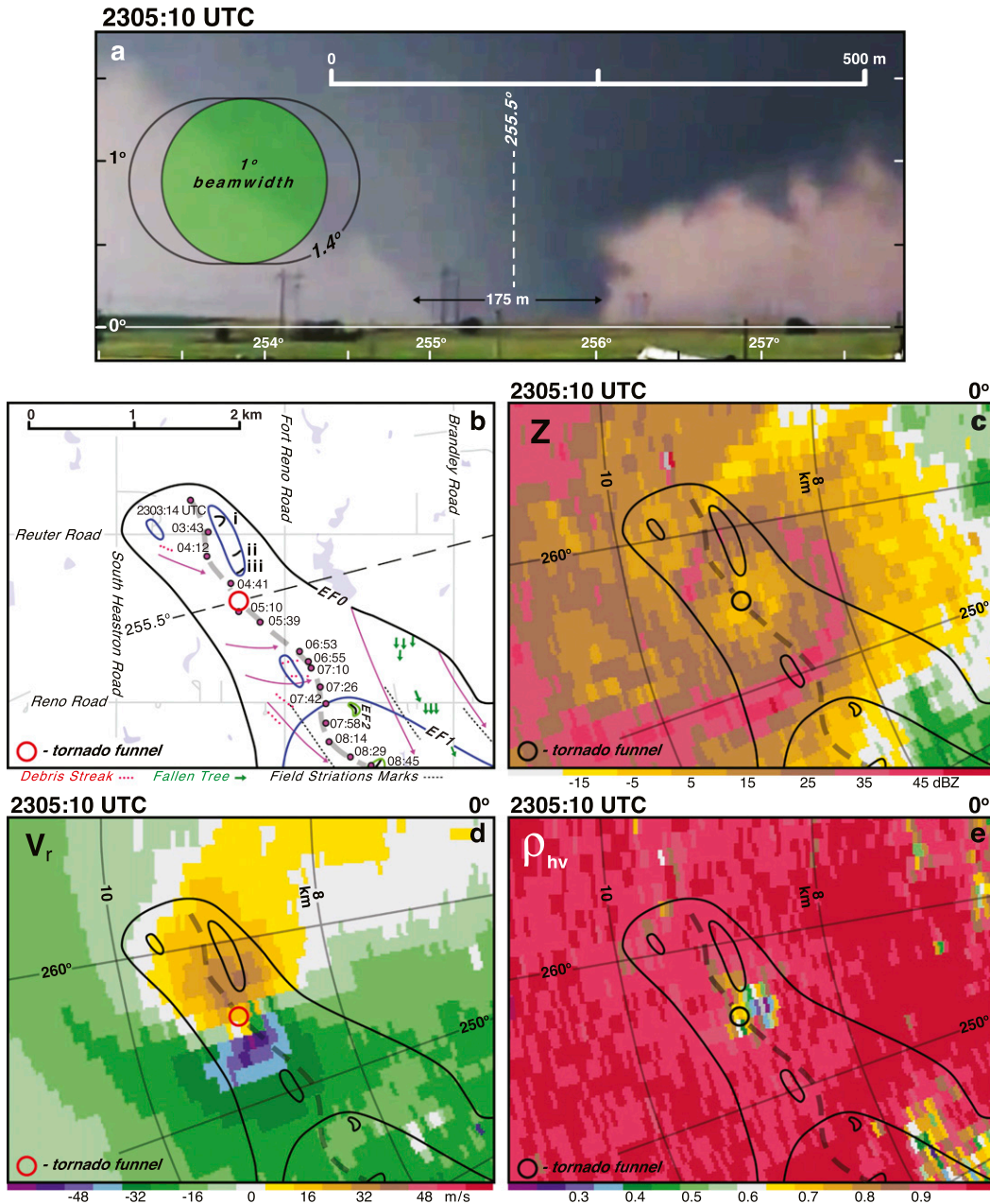


FIG. 6. (a) Photograph of tornado funnel at 2305:10 UTC. Dashed line represents the azimuth to the center of the funnel. The green circle and the larger ellipse are the 1° beamwidth and the 1.4° effective beamwidth of RaXPoI, respectively. (b) Enlargement of the damage map at the beginning of the track. EF0 and -1 contours are drawn and the dashed gray line represents the center of the tornado track. Magenta circles represent the location of the rotational couplet with the times indicated. Dashed black line is the azimuth shown in (a). Magenta lines represent the approximate flow as depicted in the damage based on fallen trees, building debris, and field striation marks. (c) Radar reflectivity, (d) single-Doppler velocity, and (e) cross-correlation coefficient ρ_{hv} at 2305:10 UTC at 0°. Red [in (b) and (d)] and black [in (c) and (e)] circles represent the location and width of the funnel. The damage track, range, and azimuth lines from RaXPoI are drawn in (c), (d), and (e). Area shown in (b) is depicted in Fig. 2.

analysis of a field the tornado traversed at ~2312 UTC (Fig. 7) reveals swirling debris and scouring marks that delineate the center of the tornado and is consistent with the location of the rotational couplet at 2312:08 UTC.

Another example is in a field south of the intersection of Reno and Reformatory Roads (Fig. 8a). A pronounced cusp in the El Reno tornado track was evident and not clearly documented in the damage survey produced by

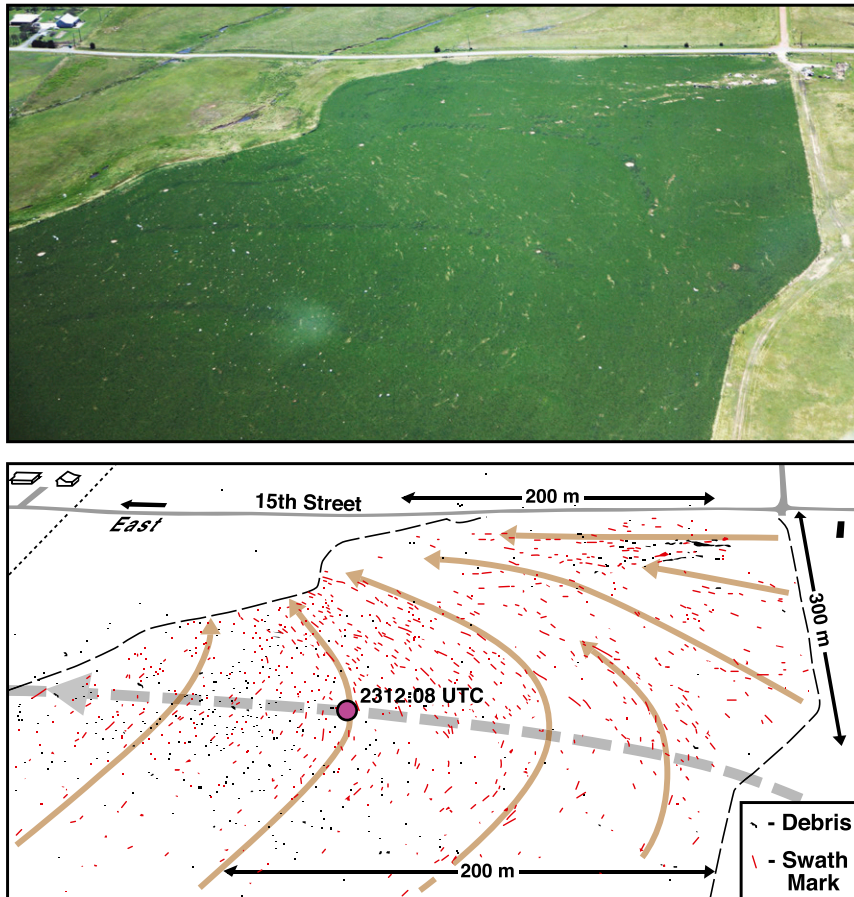


FIG. 7. (top) Aerial photo looking south of debris and scouring marks in a field is shown. (bottom) Schematic highlights both the debris (black) and scouring marks (red) visible in the top image. Brown lines represent the approximate flow as indicated by the direction of scattered debris and the scour marks. Dashed line represents approximate center of the tornado track. Magenta circle represents the location of the rotational couplet based on the Doppler velocity data recorded by RaXPol at 2312:08 UTC. Area shown in this figure is depicted in Fig. 2.

the NWS (e.g., [Bluestein et al. 2015](#), see their Fig. 8).² The cusp was readily apparent in aerial photos (Fig. 9) with a scour mark in the field that appeared analogous to an inverted “V” when viewed from the south. [Wakimoto et al. \(2003\)](#) documented a similar damage path in their study of the Kellerville, Texas, tornado during VORTEX (see their Figs. 3 and 4). The data collected by RaXPol ended at ~2315 UTC when the truck redeployed to the position near Banner Road. Accordingly, the tornado track shown after this time is based on the aerial survey (Fig. 8a). Damage marks that provided a proxy to the low-level wind were apparent in the field located west of the cusp (the dashed–dotted box

in Fig. 8a). The brown lines shown in Fig. 8a were based on lination marks in a field caused by the rolling bales of hay depicted in Fig. 10.

There are several hypotheses that could explain the cusp pattern in the damage track. [Wakimoto et al. \(2003\)](#) proposed that a tornadic vortex rotating within a larger mesocyclone circulation could produce a cusp or looping mark. Analysis of the evolution of the two circulations shown in Fig. 8 by [Bluestein et al. \(2015](#), see their Fig. 15) reveals that the El Reno tornado reached the northern tip of the cusp at approximately the same time that the smaller vortex was west of the tornado. This may suggest that the cusp is a result of the interaction between vortices around a common center ([Fujiwhara 1931](#)). As the smaller vortex rotated cyclonically from the west side to the south side around the main tornado vortex, it may have altered the trajectory

² Cusps and loops in the El Reno tornado track were also documented by [Wurman et al. \(2014\)](#).

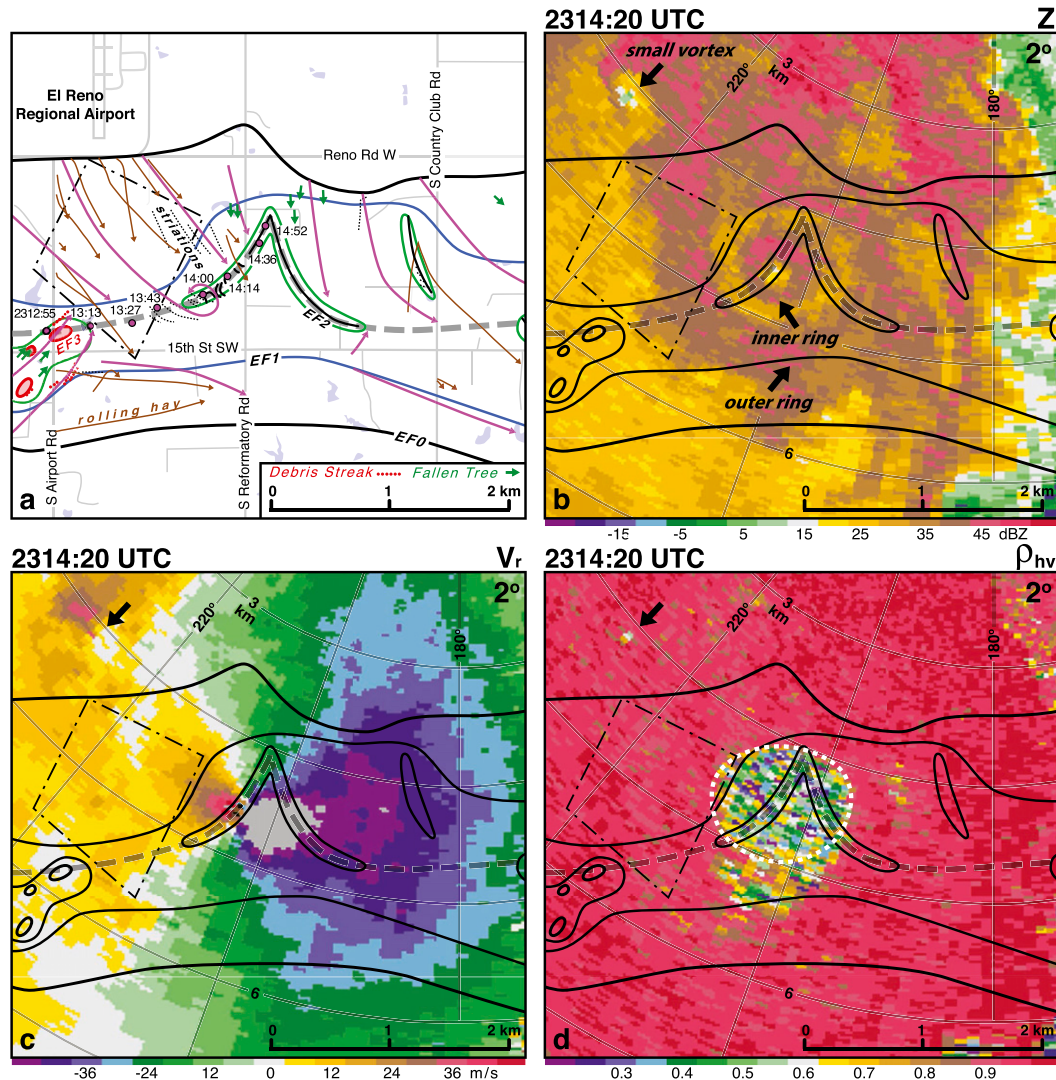


FIG. 8. Analysis at the location of the cusp in the tornado track. (a) Surface damage analysis. Black, blue, green, and red contours denote the EF0, -1, -2, and -3 damage intensity isopleths, respectively. Gray dashed line denotes the center of the tornado track. Magenta dots represent the location of the rotational couplet based on the Doppler velocity data with the times indicated. Magenta lines represent the approximate flow as depicted in the damage based on fallen trees, building debris, and streaks in the vegetation. Brown lines represent marks in the fields due to rolling bales of hay. Black lines are suction swaths marks in the field caused by the tornado. (b) Radar reflectivity, (c) Doppler velocities, and (d) ρ_{hv} at 2314:20 UTC from the RaXPoL scan at 2° . The white dashed line in (d) denotes the region inside the outer ring of enhanced radar reflectivity. The EF-scale analysis and tornado track are superimposed on (b), (c), and (d). Area enclosed by the black dashed-dotted line is shown in Fig. 10. Black arrow in (b), (c), and (d) denotes the location of a weak vortex. Gray lines in (b), (c), and (d) represent the azimuth angle and range from RaXPoL. Area shown in this figure is depicted in Fig. 2.

of the tornado to the south in a ground-relative frame of reference. A third possibility is that a surge of westerly momentum behind the rear-flank downdraft may have altered the trajectory of the tornado path in a process similar to the failed occlusion observed by Kurdzo et al. (2015, see their Fig. 14). The rolling bales of hay (Fig. 8a) could be in response to strong winds accompanying the outflow from a rear-flank downdraft.

The first appearance of a double ring of enhanced reflectivities with a weak-echo eye³ (inner and outer rings are noted in Fig. 8b) and a strong rotational couplet centered on the tornado track is shown in Fig. 8c.

³The double ring structure was also identified in radar reflectivity plots recorded at the 0° and 1° elevation-angle scans.

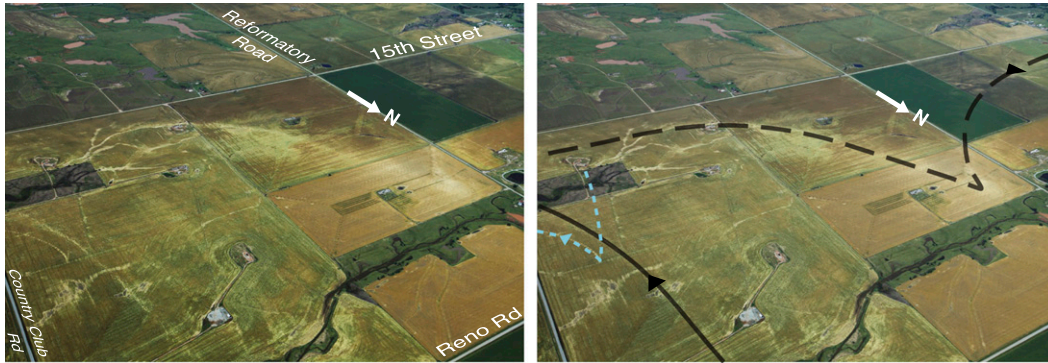


FIG. 9. Aerial photo looking southwest of the cusp in the tornado track shown in Fig. 8. Black dashed line denotes the center of the tornado track. Black line denotes a prominent swath mark located to the east of the cusp. Both features are shown in the damage map presented in Figs. 1 and 8 (highlighted by the EF2 isopleths). Dashed light blue line represents a mark in the field owing to a rolling hay bale.

Double ring structures have been previously reported in the literature (e.g., Wurman and Gill 2000; Wurman et al. 2007; Bluestein et al. 2007). These studies have concluded that the inner ring is associated with debris lofted from the ground while the outer ring is associated with precipitation. The eastern portion of the outer ring appears to be associated with a secondary maximum in radial wind speeds. The area of low ρ_{hv} delineating the lofted debris is ~ 1 km in diameter and is primarily inside the outer ring of radar reflectivity (Figs. 8b and 8d; note the white dashed line in Fig. 8d). The black arrow near the 230° azimuth in Figs. 8b–d denotes the position of another weak-echo region that is associated with a weaker cyclonic rotational couplet, discussed earlier, and a relatively small TDS. The evolution of this small vortex was shown by Wurman et al. (2014) and Bluestein et al. (2015). The aerial survey did not identify any damage indicators or ground swath marks that were caused by this smaller vortex.

d. The Weather Channel van encounter with the tornado

A crew riding in The Weather Channel vehicle driving south on Highway 81 was injured when their car was picked up and hurled by the tornado (Bettes 2014). The blue star near the intersection of Highway 81 and 15th Street denotes the final landing position of The Weather Channel vehicle (Fig. 1). Wurman et al. (2014) proposed that the vehicle was impacted and damaged by a vortex revolving around the main circulation. The track of the tornado as it moved across several fields and crossed Highway 81 was visible from the air and closely matched the locations of the rotational couplet identified in the RSDOW data (Fig. 11a). The red dot in Fig. 11a denotes the location of The Weather Channel vehicle south of the track after encountering the tornado. An enlargement of

the position of the vehicle in a field is shown in Figs. 11b and 11c. Tire tracks from a tow truck that extracted the vehicle are apparent in the figure. The dashed line (Fig. 11c) denotes the estimated trajectory of The Weather Channel vehicle once it became airborne in the intense winds. The car was traveling southbound on Highway 81 at high speed. Accordingly, the car trajectory was hypothesized to be initially southwestward before turning to the northeast. Bounce marks as the car was tumbling in the field can be readily seen in the photo and are highlighted by the red marks in Fig. 11c. The distance from the highway until the vehicle's final resting spot was ~ 100 m. The approximate intensity of the El Reno tornado in this region is shown by the black box along 15th Street (top of Fig. 11a and enlarged in Fig. 12). The aerial photo depicts EF2 and -3 damage to the few structures along 15th Street.

e. Anticyclonic tornado and loops in the tornado track

The El Reno storm spawned an anticyclonic tornado that was reported by the NWS and documented in Wurman et al. (2014) and Bluestein et al. (2015). In addition, the RSDOW scans at ~ 2320 UTC recorded an earlier anticyclonic tornado that was not reported in the NWS damage survey. An enlargement of a segment of the cyclonic tornado and the entire track of the anticyclonic tornado is shown in Fig. 13. The two counterrotating couplets can be identified in the Doppler velocity plots (highlighted by the blue circles in Fig. 13c). Enhanced reflectivity, believed to be lofted debris, encompasses the cyclonic circulation (Fig. 13b); however, this hypothesis cannot be confirmed owing to the absence of polarimetric data. The rotational couplet associated with the anticyclonic tornado was weak but the damage survey still revealed streaks of debris from a number of structures rated EF0 in damage intensity that were characterized by



FIG. 10. Aerial photo of a field north of the tornado track enclosed by the black dashed–dotted lines in Fig. 8. (right) White lines highlight the marks created by rolling bales of hay that are apparent as marks in the field (left). Thin, linear streaks that are approximately perpendicular to the hay bale marks are tracks created by trucks driving through the fields. The center of the El Reno tornado track is highlighted in the lower-left corner of the image by the gray dashed line. The magenta circle represents the location of the rotational couplet at the indicated time.

anticyclonic curvature (Fig. 13a). The times labeled along both tornado tracks illustrate that the two tornadoes were following approximately parallel tracks (Fig. 13a). Cyclonic/anticyclonic pairs of tornadoes have been documented in the past with the latter developing along the gust front separated by outflow from the rear-flank downdraft (e.g., Fujita 1981; Bluestein et al. 2007; Tanamachi et al. 2012; Wurman and Kosiba 2013, Bluestein et al. 2016). The magenta lines, which delineate the direction of fallen trees, debris streaks from structures, and swath marks in the fields support the presence of a rear-flank outflow between the two tornadoes (Fig. 13a).

Wurman et al. (2014) presented radar evidence of two prominent loops in the El Reno tornado track separated by ~ 1.7 km. The loops and the location of the rotational couplets along the damage track are presented in Fig. 14a. The second loop near the intersection of Reuter and Radio Roads was near the location where several storm chasers were killed while collecting data on the tornado (Wurman et al. 2014). A blue star in Fig. 1 denotes the location where their researcher's vehicle came to rest northeast of the intersection of Reuter and Radio Roads. Aerial photos of the wheat field where the northern loop occurred clearly reveal the tornado track as a boundary between light and dark shaded regions (Fig. 14b and highlighted by the blue dashed line in Fig. 14c). The change in shading is due to a discontinuity in albedo caused by matted vegetation aligned in different directions.

f. Multiple vortex structure near the end of the tornado track

The tornado's translational speed slowed after it crossed Interstate 40 (Fig. 1). Subsequently, the tornado

turned to the east before dissipating near Banner Road. A number of structures were impacted and damage indicators in several areas were rated EF3 intensity. The aerial survey documented numerous downed trees, scattered debris from structures, and swath marks in open fields (Fig. 15a). At least seven rotational couplets/shear features are apparent in the low-level scan of single-Doppler velocities at 2327:50 UTC (Fig. 15c), highlighting the multiple vortex structure of the El Reno tornado discussed by Snyder and Bluestein (2014) and Wurman et al. (2014). Several of the couplets are associated with regions of enhanced radar reflectivity (Fig. 15b) suggesting lofted debris. The eastern rotational couplet located south of Interstate 40 was particularly intense and may have produced the pronounced swath mark in a field as it translated southeast to Manning Road (Figs. 15a and 15e). A pronounced ring of relatively high values of σ_v (highlighted by the dashed circle in Fig. 15d) is close to the location of the rotational couplets.

g. Detailed analysis of a suction vortex

A prominent suction vortex was noted in both photographs and high-definition video during the time that RaXPol was deployed at site 2 (Fig. 16). This feature has been discussed by Snyder and Bluestein (2014, see their Figs. 8 and 9) and Wurman et al. (2014). The suction vortex was first identified along the southern periphery of the El Reno tornado and, subsequently, translated rapidly from south to north relative to the visible funnel (Fig. 16). The speed of the suction vortex around the periphery of the El Reno tornado was estimated to be 76.7 m s^{-1} , consistent with the calculations by Snyder

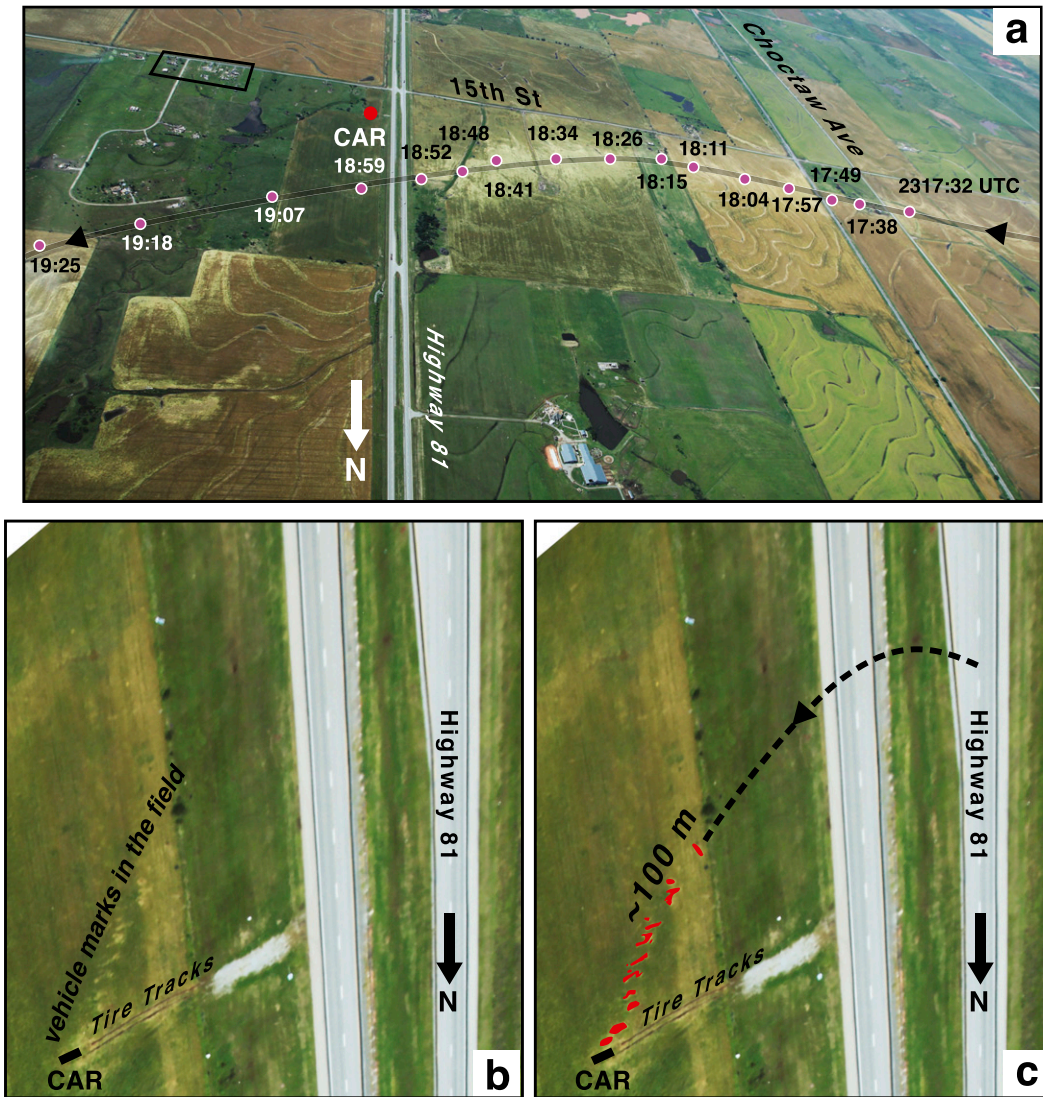


FIG. 11. (a) A photo looking south at the tornado track as it crossed Highway 81. The track is highlighted by the gray line. Magenta dots are the locations of the rotational couplet based on Doppler velocity data recorded by RSDOW with the times indicated. Red dot represents the location where The Weather Channel car was found. Small black box near the top-left corner is enlarged in Fig. 12. (b) Enlarged area where the car was found. Bounce marks and the tire tracks from a tow truck are labeled on the figure. (c) Same area as shown in (b). Red markings highlight the location of the bounce marks shown in (b). The black dashed line represents the approximate trajectory of the car after being blown off the southbound lanes of Highway 81. The final location of the car is shown by the black rectangle. Area shown in (a) is depicted in Fig. 2.

and Bluestein (2014) and Wurman et al. (2014). The location of the suction vortex (red dashed line in Fig. 1) was determined by a combination of RaXPOL data and a photogrammetric analysis of the suction vortex in high-resolution video and photographs.

A damage swath from the vortex based on the aerial survey is apparent in Fig. 17a and is highlighted by the dashed magenta line in Fig. 17b. The azimuths (white dashed lines) to the center of the suction vortex are

based on photogrammetry calculations (Fig. 16). In addition, the locations of the rotational couplet (black crosses) have been added to Fig. 17b. This is believed to be the first time that a funnel associated with a suction vortex visually apparent in photographs and video has been unambiguously resolved in Doppler radar data and appears to be associated with a swath mark in a field. Two structures located southwest of the intersection of Evans and Jensen Roads (near the 255° azimuth in



FIG. 12. An aerial photo looking north of a region depicting EF2 and -3 damage associated with the El Reno tornado. The location of the photo (shown in Fig. 11a) is ~ 500 m east of the intersection of Highway 81 and 15th Street.

Fig. 16b) were directly in the path of the suction vortex. The damage to both structures was rated EF2 (Fig. 17c); however, it could not be determined if the observed damage was a result of the overall tornadic circulation or the suction vortex (or a combination of both).

4. Dual-Doppler analysis from two rapid-scan radars

The deployment of the RaXPOL and RSDOW on the El Reno storm provided an opportunity to perform a dual-Doppler analysis using two rapid-scan radars for three consecutive times (2324:39, 2324:54, and 2325:11 UTC) when the tornado was located near the intersection of Radio and Reuter Roads. Strong surface wind damage rated EF2 was identified at two locations northwest and east of the intersection of Radio and Reuter Roads during the wind syntheses time (Fig. 18a). This is also close to the time that the storm chasers' vehicle that resulted in fatalities was approaching its final landing spot northeast of the intersection (shown by the red dot in Fig. 18) as described by Wurman et al. (2014). As previously mentioned, this analysis time was near the location where some of the most intense Doppler velocities were measured (Wurman et al. 2014; Snyder and Bluestein 2014).

The three consecutive volume scans collected by RaXPOL contained six elevation angles (0° , 1° , 2° , 3° , 4° , and 5°). The data for the 0.5° elevation angle were recorded by RSDOW; however, the data for the 1.5° elevation angle were missing. The data collected by RSDOW in the analysis domain at the next elevation angle (2.5°) were located above the level at which RaXPOL was scanning. Accordingly, the wind synthesis was only created for one level (175 m above the RaXPOL location; ARL) in the present case. The range to the tornado was ~ 5 and 12 km from the RaXPOL and

RSDOW radar locations, respectively. The El Reno tornado was moving at $\sim 17 \text{ m s}^{-1}$ during this period. The viewing angles of the radars near the center of the tornado intersect at $\sim 50^\circ$ (Fig. 1). The grid spacing (85 m) was based on the coarsest data spacing using the azimuthal resolution associated with RSDOW. A two-pass Barnes filter (Barnes 1964) was applied using a smoothing parameter $\kappa = (1.33\Delta)^2$, where Δ equals the grid spacing (Pauley and Wu 1990). The response function resulted in 30% and 10% of the energy at wavelengths equal to and less than 0.35 and 0.5 km, respectively, being damped. The interested reader is referred to Majcen et al. (2008) for additional information regarding the filtering process. It should be noted that any suction vortex present in the analysis domain would be highly damped by the filtering routine. The ground-relative rather than tornado-relative wind field is presented in order to facilitate comparisons with the damage survey.

Interpolated radar reflectivity from RaXPOL is shown in Figs. 18b and 18d; however, the finescale details of the single-Doppler velocities (Fig. 18c), ρ_{hv} (Fig. 19a), and Z_{DR} (Fig. 19c) fields are shown by presenting the raw scans from the RaXPOL at an elevation angle of 1° . The $1 \times 10^{-1} \text{ s}^{-1}$ isopleth of vertical vorticity (ζ) nearly encircles the ring of high radar reflectivity accompanying the hook echo (Fig. 18b). The peak ζ is greater than $3 \times 10^{-1} \text{ s}^{-1}$, is located in the weak-echo hole (WEH) of the hook echo, and is centered on the rotational couplet (Fig. 18c). The maximum is also located in the western sector of a region rated EF2 in damage intensity and close to the location where the storm chasers' vehicle was recovered (Figs. 18a and 18b). The magnitude of the dual-Doppler wind fields at low levels (Fig. 19d) suggests a wavenumber-2 pattern (also apparent in a plot of the tangential winds; not shown) with peak wind speeds $> 90 \text{ m s}^{-1}$ (maximum gridpoint value was 95 m s^{-1}) and 60 m s^{-1} in the southeastern and northern quadrants relative to the center of the circulation, respectively. Noteworthy is the area enclosed by the 90 m s^{-1} isopleth in the filtered dual-Doppler wind synthesis (Fig. 19d) that exceeds the minimum value for EF5 damage intensity (89 m s^{-1}). The relationship between surface wind speeds and Doppler velocities recorded by radars has been an ongoing topic of discussion in the literature (e.g., Kosiba and Wurman 2013; Wurman et al. 2013). The situation is complicated in the present case since the intense, low-level Doppler velocities within the El Reno tornado occurred over open terrain with few damage indicators (Marshall et al. 2014; Snyder and Bluestein 2014). Accordingly, it is possible that maximum wind speeds exceeding an EF2 rating could have occurred in the area located east of the

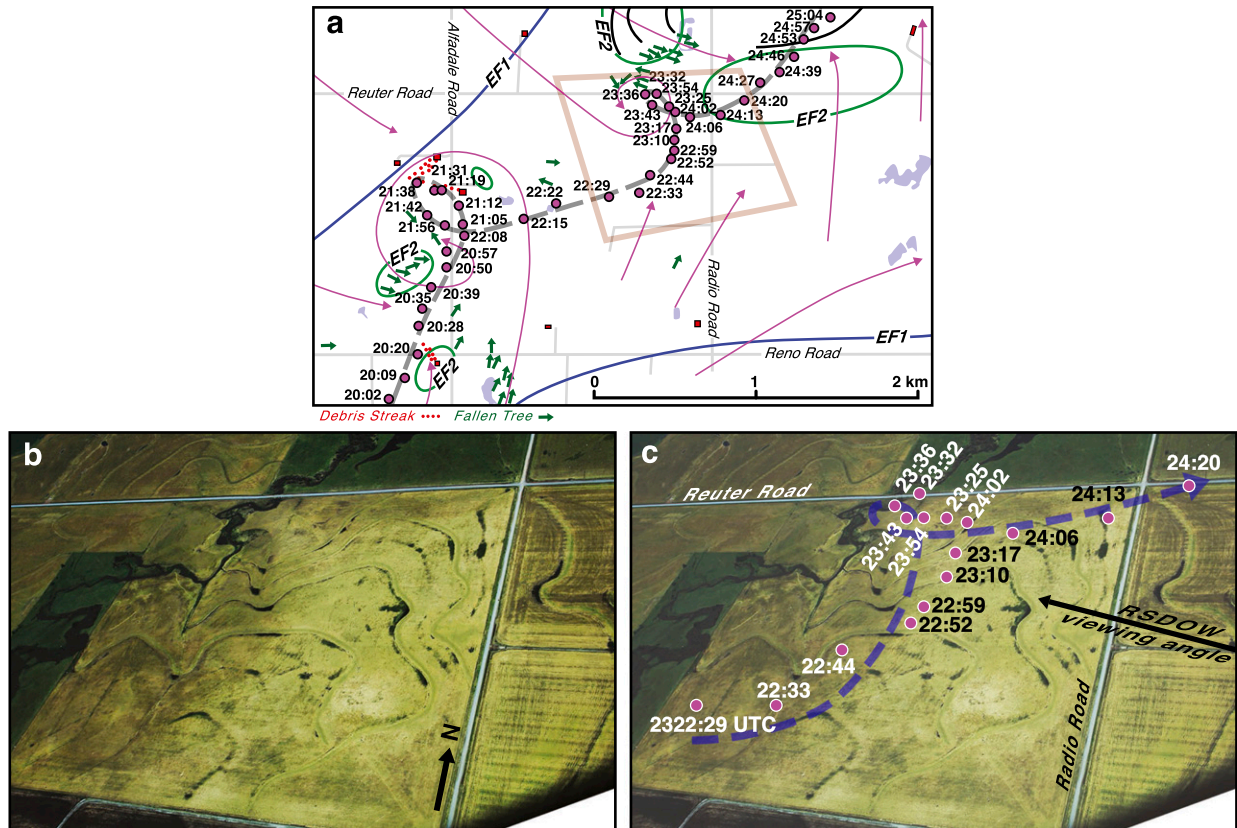


FIG. 14. (a) Surface analysis of the damage track during the period when the tornado made two loops. Blue and green contours denote the EF1 and -2 damage intensity isopleths, respectively. Dashed gray line denotes the center of the tornado track. Magenta dots represent the times and location of the rotational couplets based on Doppler velocity data recorded by RSDOW. Magenta lines represent the approximate flow as depicted by fallen trees and building debris. Black lines are suction swaths marks in the field caused by the tornado. Area shown in the figure is depicted in Fig. 2. Brown box in the figure is enlarged in (b) and (c). (b) An aerial photo looking north of a loop in the tornado track west of the intersection of Reuter and Radio Roads. (c) Blue dashed line superimposed onto the aerial photo represents the tornado track. The magenta circles represent the locations of the rotational couplet based on the Doppler velocity recorded by RSDOW. The view angle of RSDOW is shown by the black arrow.

intersection of Reuter and Radio Roads. The regions of strong positive and negative tornado-relative radial velocities (U), based on a center defined by the maximum ζ , are located northeast and southwest of the circulation center, respectively (Fig. 18d).

An important assumption when performing a kinematic analysis of Doppler velocities is that the scatterers are moving with the horizontal wind field. It is widely recognized, however, that hydrometeors and lofted debris within tornadoes can undergo centrifuging, which produces a positive bias in the tornado-relative radial velocity calculations (e.g., Wurman and Gill 2000; Dowell et al. 2005; Lee and Wurman 2005). Unfortunately, quantitative assessments of the centrifuging effect have been rarely documented in the refereed literature (Wakimoto et al. 2012; Kosiba and Wurman 2013; Nolan 2013). There are several distinct bands of convergence that are evident in Figs. 19a and 19b. One

convergence band (yellow dashed line in Fig. 19a) denotes the position of an internal or secondary rear-flank gust front (e.g., Wurman et al. 2007; Marquis et al. 2008; Karstens et al. 2010; Lee et al. 2012). The gust front is positioned along the southern edge of the ridge of higher Z_{DR} (Fig. 19c). Large Z_{DR} and $\rho_{hv} > 0.95$ suggest the presence of hydrometeors (e.g., Palmer et al. 2011). The Z_{DR} ridge is also located within a zone of strong wind speeds (Figs. 19c and 19d) with the peak speeds located near the eastern tip of the ridge. The strong speeds suggest that the hydrometeors are being rapidly advected around the southern periphery of the hook echo and the TDS.

The analyses presented in Figs. 19c and 19d appear to be in contrast to the findings presented by Kumjian (2011, see his Fig. 10) and French et al. (2015). They suggest that rear-flank downdrafts associated with tornadic hook echoes are accompanied by relatively low

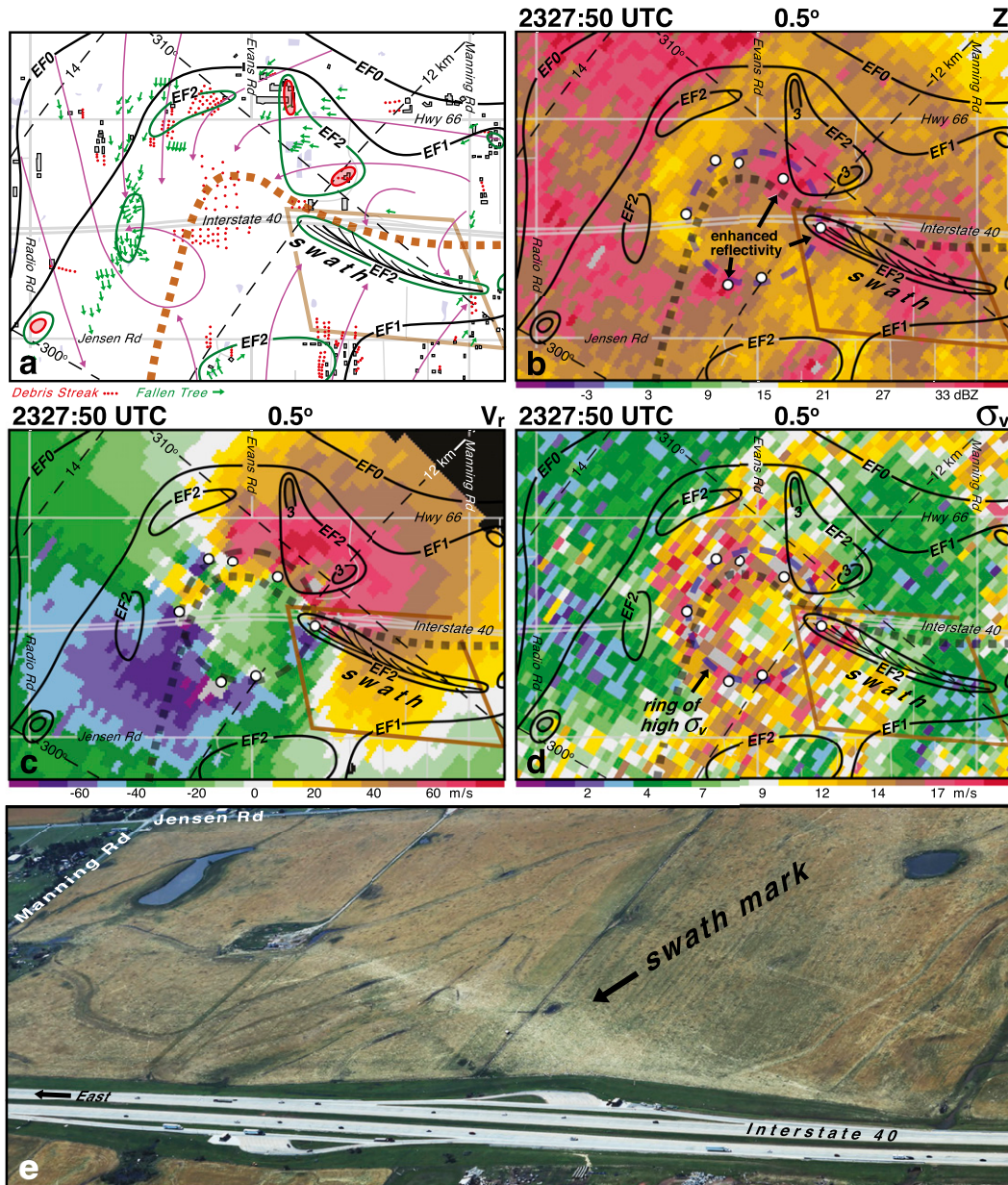


FIG. 15. (a) Enlargement of the damage map near Interstate 40. EF0, -1, -2, and -3 damage intensity isopleths are drawn and the dashed brown line represents the approximate center of the tornado track. Magenta lines represent the approximate flow as depicted by fallen trees and building debris. Black lines are suction swaths marks in the field caused by the tornado. (b) Radar reflectivity scan at 2327:50 UTC at 0.5°. (c) Single-Doppler velocity scan at 2327:50 UTC at 0.5°. (d) Spectral width scan at 2327:50 UTC at 0.5°. (e) Aerial photograph of the suction swath mark located in a field south of Interstate 40. The area encompassed in the photograph is shown by the brown box in (a),(b),(c), and (d). The tornado track and EF isopleths are superimposed on (b),(c), and (d). The small, white circles drawn on (b),(c), and (d) denote the locations of rotational couplets. The dashed circle drawn on (b), (c), and (d) denotes a ring of relatively high values of σ_v . Dashed black lines in (a),(b),(c), and (d) are range and azimuth angles from RSDOW. Area shown in (a) is depicted in Fig. 2.

2325:56 UTC

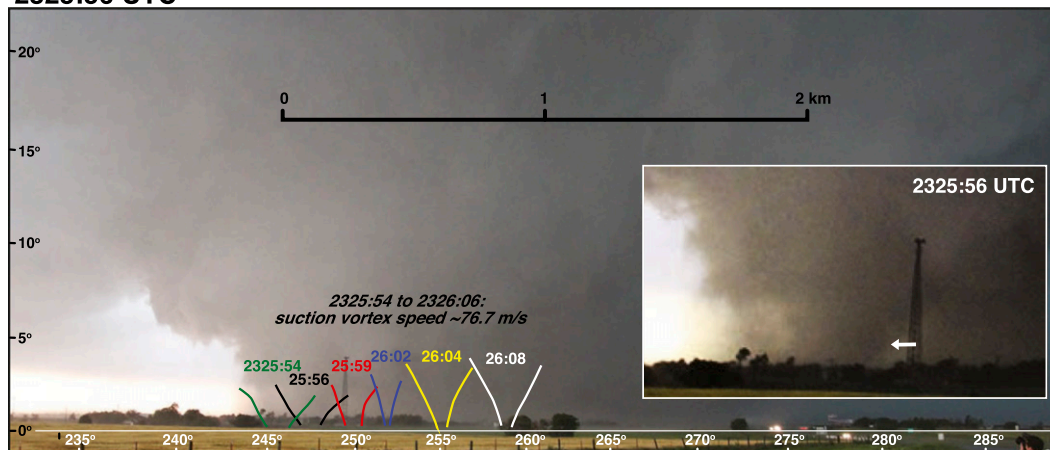


FIG. 16. Photogrammetric analysis of the El Reno tornado at 2325:56 UTC depicting the progression of a suction vortex relative to the condensation funnel. Color lines represent the outline of the suction vortex at different times based on a high-definition video taken from the RaXPOL site near Banner Road. The inset is an enlargement of the suction vortex at 2325:56 UTC. Length scale is valid at the distance of the suction vortex.

Z_{DR} associated with small drops generated by warm rain processes and are transported to the surface in dynamically forced downdrafts. Although there are regions within the rear-flank outflow to the south of the gust front that are characterized by low Z_{DR} , the Z_{DR} ridge occupies a significant portion of the outflow.

It would be expected that the pockets of dust/debris located south of the tornado funnel discussed in Wakimoto et al. (2015, see their Fig. 13) might align along the gust front (e.g., Kurdzo et al. 2015); however, the extension of the line of low ρ_{hv} shown in Fig. 19a extends to the south of the convergence band. It should be noted that data collected during the 0° scan suggests that another band of low ρ_{hv} near the surface more closely aligns along the gust front (not shown).

The dual-Doppler wind synthesis resolved two additional convergence zones denoted by the black and white dashed lines (Fig. 19a). An inner band (black dash line) completely encircles the ring of high radar reflectivity (Fig. 18b). An outer band of convergence (white dashed line) extends north and then northeastward from the western segment of the inner band. The western, southern, and eastern portions of the inner band combined with the outer band are nearly coincident with the outer boundary of the TDS (Fig. 19a). There are two possible explanations for this coincidence. The convergence band could be a result of the aforementioned positive bias in tornado-relative radial velocity owing to centrifuging of the vast amounts of lofted debris swirling within the El Reno tornado. Accordingly, the convergence zone is an artifact of the difference between the wind and debris velocities

measured by RaXPOL. An alternative explanation is that the convergence band is not an artifact but is a feature that has formed at the outer edge of the debris field and is possibly generating updrafts, owing to the convergence, that surround the TDS. These hypotheses will be examined for both the inner and outer bands.

The northern segment of the inner band of convergence is not located at the outer boundary of the TDS. Instead, the band extends across the TDS and is located near the northern periphery of the high radar reflectivity ring and the radius of maximum wind speeds. The band's location suggests that there are relatively large debris particles that are being lofted and strongly centrifuged out to a range slightly beyond the hook echo. Accordingly, the inner convergence band is believed to be a result of the positive bias in the tornado-relative radial velocities. The region of the TDS located between the outer and inner band is hypothesized to be composed of relatively small lofted debris since the radar reflectivities and ρ_{hv} are relatively low. It is possible that the outer band of convergence is another artifact created by centrifuging of lofted debris owing to its location at the periphery of the TDS. Another, more likely, scenario is that the region between the outer and inner bands is characterized by strong inflow of small debris particles and dust north of the hook echo (shown schematically by the gray arrow in Fig. 19a). As a result, the outer convergence band may be the region where the inflow transitions into the storm updraft. Support for this hypothesis is the absence of a convergence zone in the northeast quadrant of the TDS. Instead, there is a transition from a

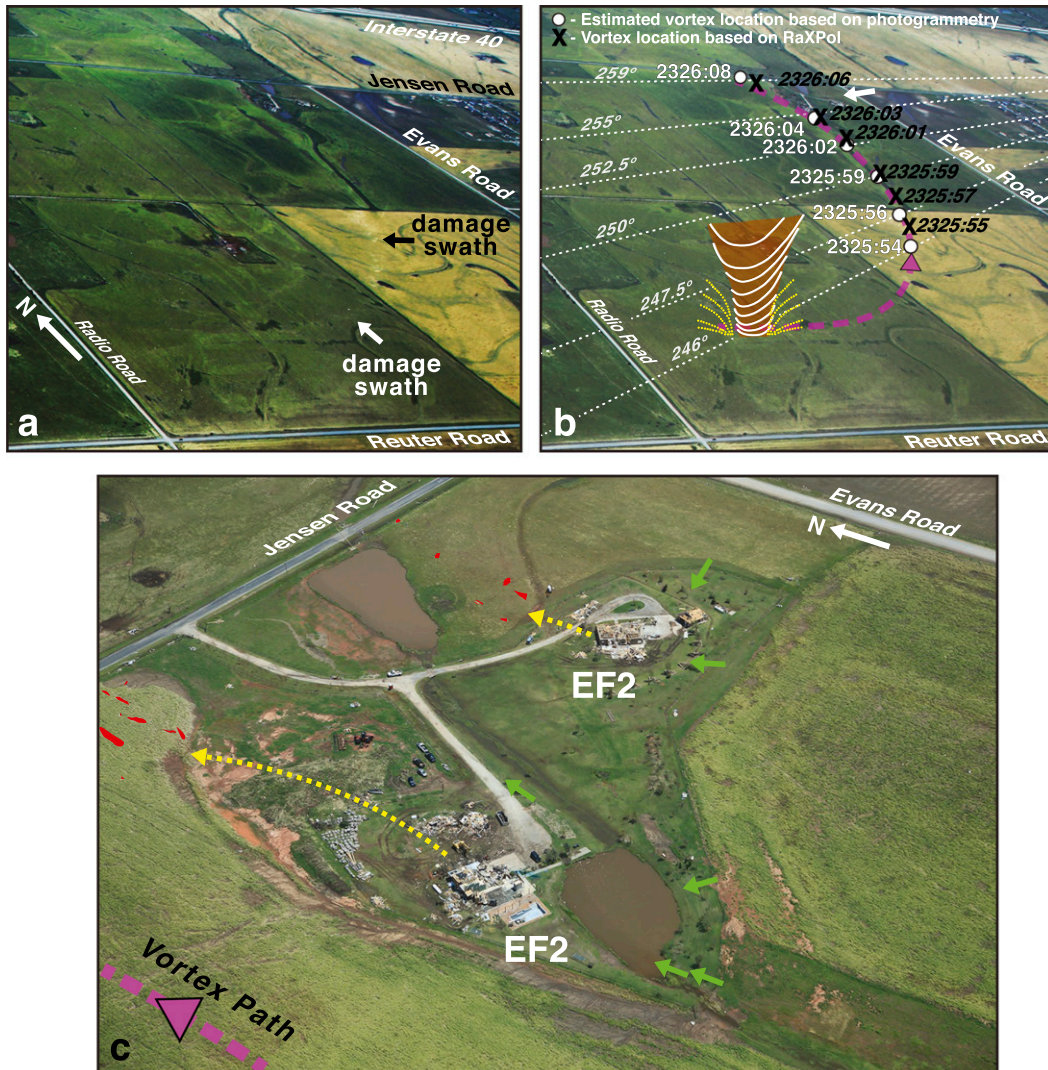


FIG. 17. (a) Aerial photo of the field where the suction vortex created a damage swath (black and white arrows). (b) Same photo as shown in (a). Dashed magenta line denotes the location of the damage swath. Black crisscrosses denote the locations of the rotational couplet based on Doppler velocity data with the times indicated. White circles represent the approximate locations of the suction vortex based on high-definition video. Dashed white lines represent azimuth angles from RaXPoI. White arrow in (b) denotes the location that is enlarged in (c). (c) EF2 damage caused by the suction vortex as it passed near two houses located southwest of the intersection of Jensen and Evans Roads. Dashed magenta line represents the path of the suction vortex. Green arrows represent the direction of fallen trees. Red areas represent the location of building debris with the trajectory indicated by the dashed yellow lines. Area shown in (a) is depicted in Fig. 2.

wedge of relatively low ρ_{hv} (near the head of the gray arrow in Fig. 19a) to high ρ_{hv} farther to the east with widely dispersed isolated pockets of low ρ_{hv} (near the tail of the gray arrow). The latter may outline a region where the inflow reaches a minimum wind speed to loft dust and small debris. Strong inflow transitioning into an updraft within the weak-echo notch of the hook echo has been well documented in the literature (e.g., Browning 1964; Lemon and Doswell 1979).

Many of the features noted earlier are apparent in the wind synthesis at 2325:11 UTC (Figs. 20 and 21), with several notable differences. The location of the maximum in vertical vorticity appears as an arc (note the $2 \times 10^{-1} \text{ s}^{-1}$ isopleth) and is nearly collocated with the southeastern portion of the ring of high radar reflectivity rather than being centered within the WEH (Fig. 20b). This vorticity pattern might suggest the presence of suction vortices, which is supported by the location of

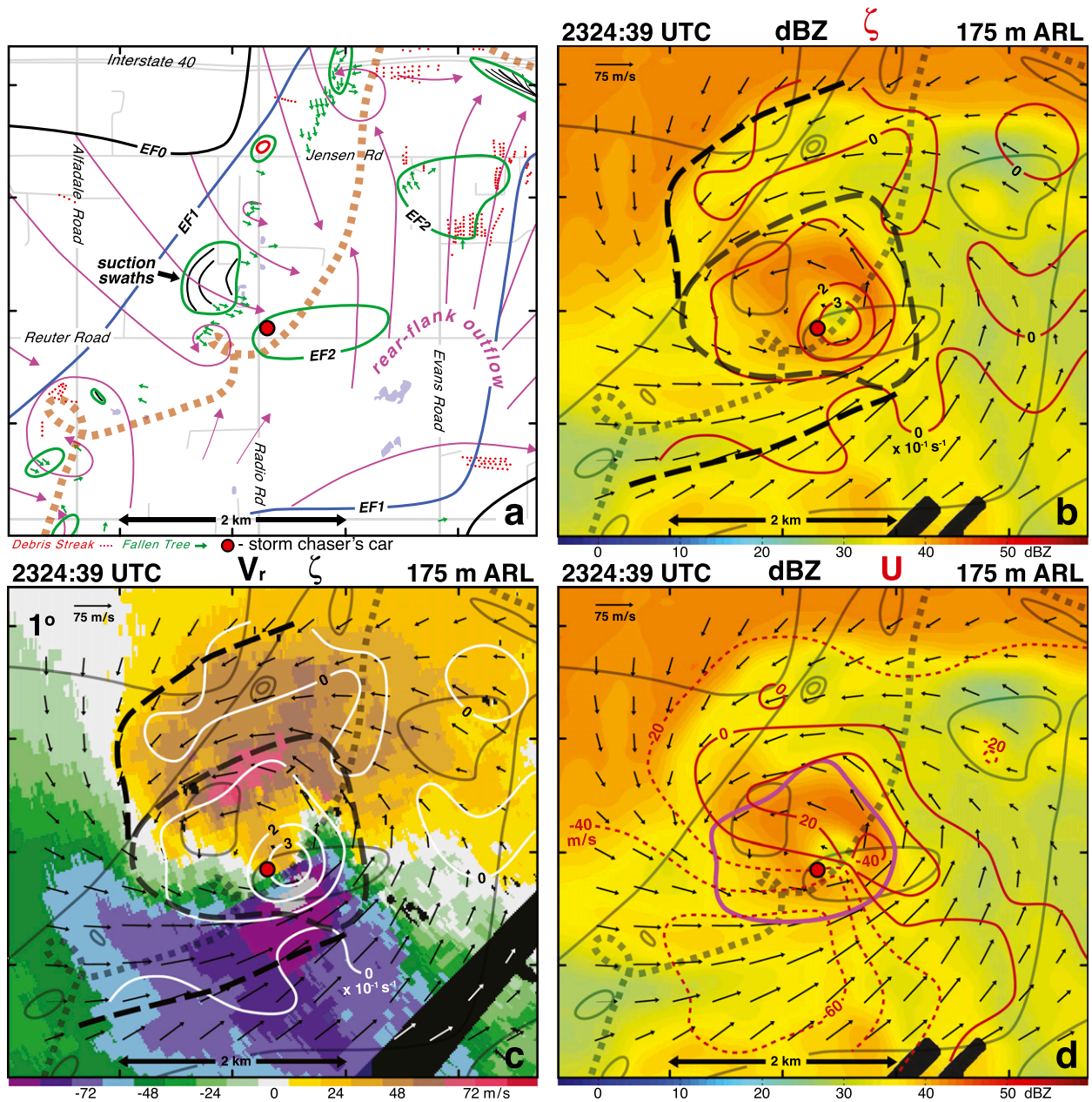


FIG. 18. (a) Enlargement of the damage map in the region where dual-Doppler data were collected by RSDOW and RaXPOL. EF0, -1, -2, and -3 damage intensity isopleths are drawn as black, blue, green, and red lines, respectively. The brown dashed line represents the center of the tornado track. Magenta lines represent the approximate flow as depicted in the damage based on fallen trees, building debris, and streaks in the vegetation. The dual-Doppler analysis at 2324:39 UTC at a height of 175 m ARL is presented in subsequent panels. (b) Radar reflectivity, vertical vorticity ($\times 10^{-1} \text{ s}^{-1}$), and the ground-relative wind field. The EF isopleths and center of the tornado track are superimposed as gray lines. Long, dashed lines represent zones of maximum low-level convergence. (c) Single-Doppler velocities, vertical vorticity ($\times 10^{-1} \text{ s}^{-1}$), and the ground-relative wind field. Vertical vorticity ($\times 10^{-1} \text{ s}^{-1}$) are drawn as white lines. The EF isopleths and center of the tornado track are superimposed as gray lines. Long, dashed lines represent zones of maximum low-level convergence. (d) Radar reflectivity and the ground-relative wind field. Isopleths of tornado-relative radial velocity U are shown as solid (positive) and dashed (negative) red lines, respectively. The EF isopleths and center of the tornado track are superimposed as gray lines. The $1 \times 10^{-1} \text{ s}^{-1}$ isopleth of vertical vorticity is drawn as a magenta line. The radar reflectivity plot at 175 m ARL is shown in (b) and (d). The RaXPOL scan at 1° elevation angle for single-Doppler velocities is shown in (c). The red dot near the intersection of Reuter and Radio Roads is the final location of a storm chaser car that resulted in fatalities and is shown on all panels. Area shown in the figure is depicted in Fig. 2.

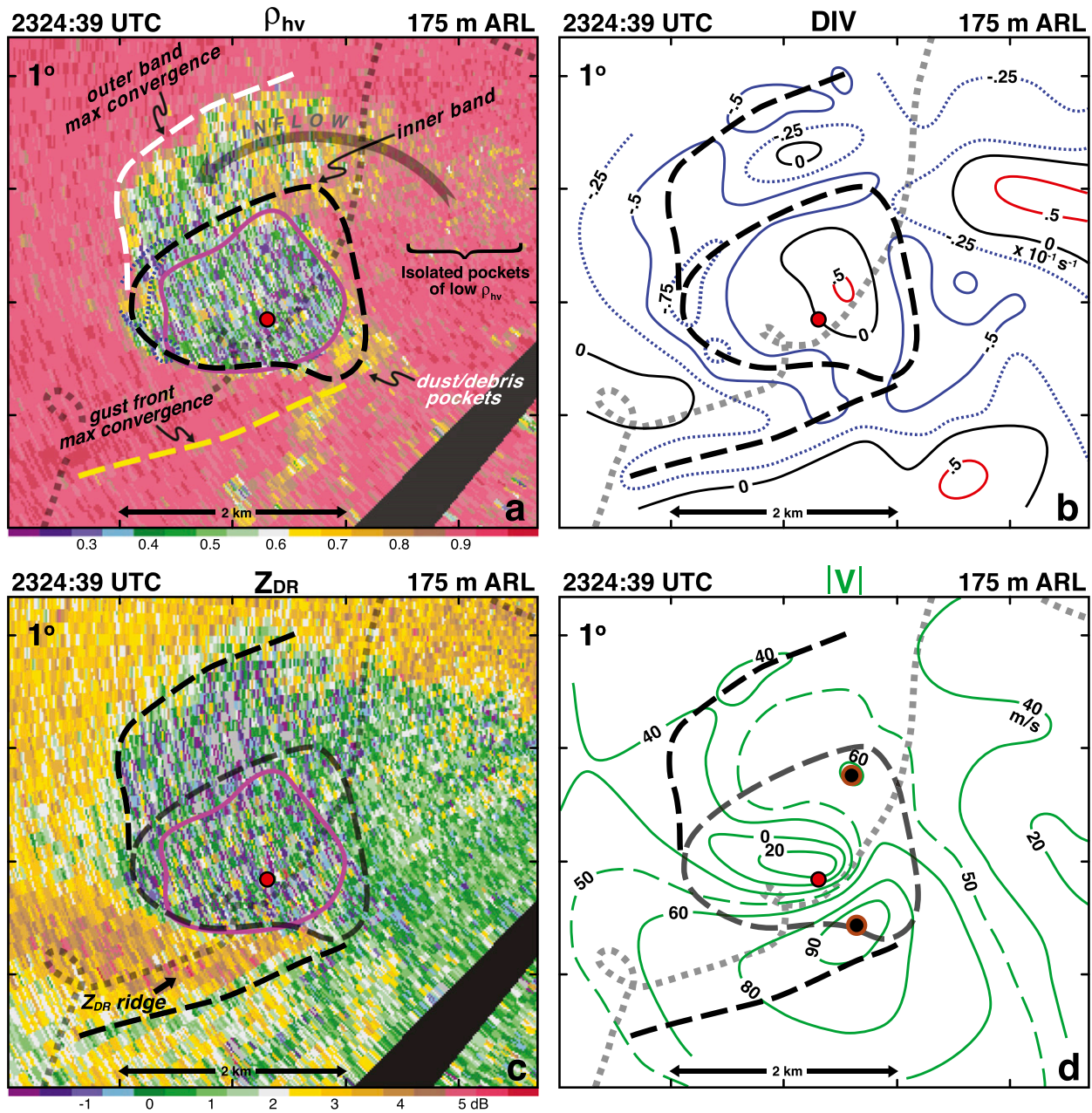


FIG. 19. (a) The ρ_{hv} at 2324:39 UTC (1° elevation angle) from RaXPol. The long, dashed lines (white, black, and yellow) represent zones of maximum low-level convergence. The $1 \times 10^{-1} \text{ s}^{-1}$ isopleth of vertical vorticity is drawn as a magenta line. (b) Low-level divergence fields ($\times 10^{-1} \text{ s}^{-1}$). Divergence and convergence isopleths are drawn as red and blue lines, respectively. The -0.25 and $-0.75 \times 10^{-1} \text{ s}^{-1}$ isopleths of convergence have been added as dashed blue lines. The long, dashed lines represent zones of maximum low-level convergence. (c) The Z_{DR} at 2324:39 UTC (1° elevation angle) from RaXPol. The long, dashed lines represent zones of maximum low-level convergence. The $1 \times 10^{-1} \text{ s}^{-1}$ isopleth of vertical vorticity is drawn as a magenta line. (d) Magnitude of the ground-relative wind field. Isopleths of the wind speed are drawn as green lines. The 50 m s^{-1} isopleth of wind speed has been added as a dashed green line. The brown circles in (d) denote the location of the maximum speed. The red dot is the final location of a storm chaser car that resulted in fatalities and is shown on all panels. Area shown in the figure is depicted in Fig. 2.

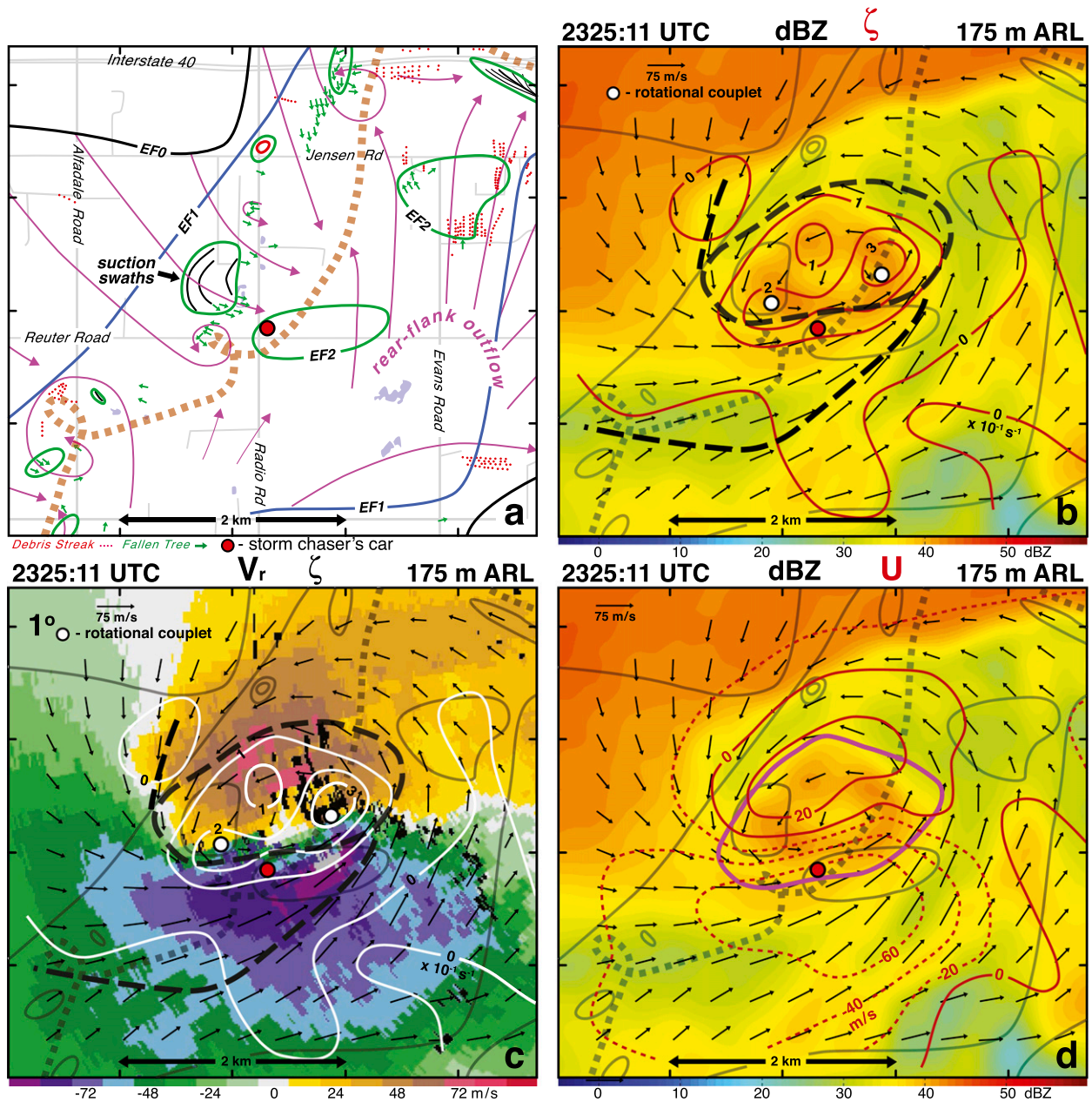


FIG. 20. (a) Enlargement of the damage map in the region where dual-Doppler data were collected by RSDOW and RaXPol. EF0, -1, -2, and -3 damage intensity isopleths are drawn as black, blue, green, and red lines, respectively. The brown dashed line represents the center of the tornado track. Magenta lines represent the approximate flow as depicted in the damage based on fallen trees, building debris, and streaks in the vegetation. The dual-Doppler analysis at 2325:11 UTC at a height of 175 m AGL is presented in subsequent panels. (b) Radar reflectivity, vertical vorticity ($\times 10^{-1} \text{ s}^{-1}$), and the ground-relative wind field. The EF isopleths and center of the tornado track are superimposed as gray lines. Long, dashed lines represent zones of maximum low-level convergence. (c) Single-Doppler velocities, vertical vorticity ($\times 10^{-1} \text{ s}^{-1}$), and the ground-relative wind field. Vertical vorticity ($\times 10^{-1} \text{ s}^{-1}$) are drawn as white lines. The EF isopleths and center of the tornado track are superimposed as gray lines. Long, dashed lines represent zones of maximum low-level convergence. (d) Radar reflectivity and the ground-relative wind field. Isopleths of tornado-relative radial velocity U are shown as solid (positive) and dashed (negative) red lines, respectively. The EF isopleths and center of the tornado track are superimposed as gray lines. The $1 \times 10^{-1} \text{ s}^{-1}$ isopleth of vertical vorticity is drawn as a magenta line. The radar reflectivity plot at 175 m ARL is shown in (b) and (d). The RaXPol scan at 1° elevation angle for single-Doppler velocities is shown in (c). The red dot near the intersection of Reuter and Radio Roads is the final location of a storm chaser car that resulted in fatalities and is shown on all panels. Area shown in the figure is depicted in Fig. 2.

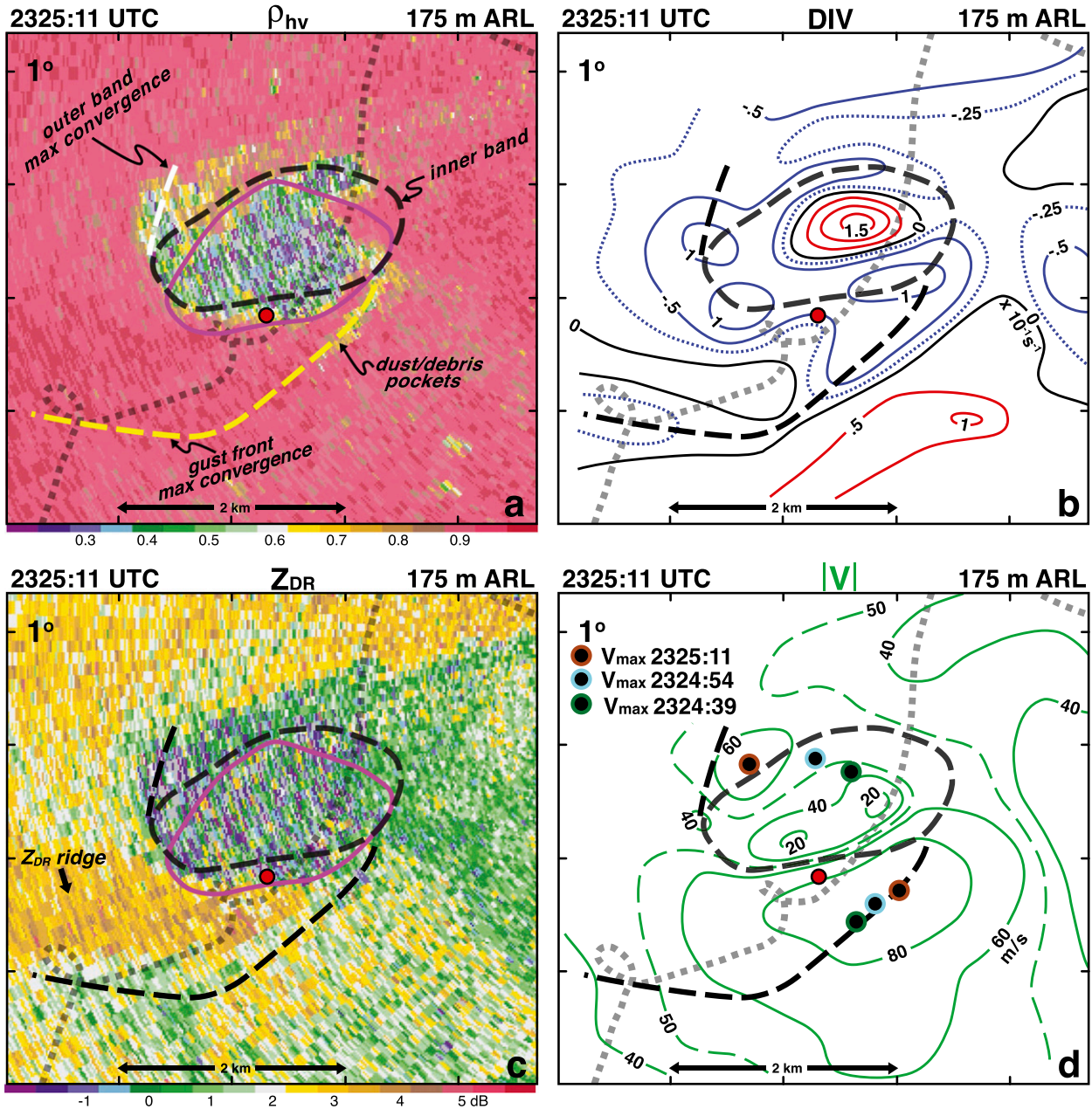


FIG. 21. (a) The ρ_{hv} at 2325:11 UTC (1° elevation angle) from RaXPol. The long, dashed lines (white, black, and yellow) represent zones of maximum low-level convergence. The $1 \times 10^{-1} \text{ s}^{-1}$ isopleth of vertical vorticity is drawn as a magenta line. (b) Low-level divergence fields ($\times 10^{-1} \text{ s}^{-1}$). Divergence and convergence isopleths are drawn as red and blues lines, respectively. The $-0.25 \times 10^{-1} \text{ s}^{-1}$ isopleths of convergence have been added as dashed blue lines. The long, dashed lines represent zones of maximum low-level convergence. (c) The Z_{DR} at 2325:11 UTC (1° elevation angle) from RaXPol. The long, dashed lines represent zones of maximum low-level convergence. The $1 \times 10^{-1} \text{ s}^{-1}$ isopleth of vertical vorticity is drawn as a magenta line. (d) Magnitude of the ground-relative wind field. Isopleths of the wind speed are drawn as green lines. The 50 m s^{-1} isopleth of wind speed has been added as a dashed green line. The brown circles in (d) denote the location of the maximum speed at the 2325:11 UTC analysis time. Green and blue circles denote the locations of the maximum speed at the previous analysis times. The red dot is the final location of a storm chaser car that resulted in fatalities and is shown on all panels. Area shown in the figure is depicted in Fig. 2.

two rotational couplets (white circles in Figs. 20b and 20c). The pattern of tornado-relative radial velocities (Fig. 20d) is similar to the earlier analysis time (Fig. 18d) although the isopleths have rotated in a counterclockwise direction relative to the WEH. This counterclockwise rotation is also apparent in the plot of the magnitude of the wind field (Fig. 21d). The three colored circles shown in Fig. 21d represent the locations of the peak wind speed in the wavenumber-2 pattern for the three dual-Doppler analysis times. The strong winds encircled by the 80 m s^{-1} isopleth rotating around the eastern side of the hook echo were a contributing factor in the damage pattern labeled rear-flank outflow based on the aerial survey (Fig. 20a).

The band of maximum convergence along the internal rear-flank gust front at 2325:11 UTC is apparent and it continues to align along the southern edge of the Z_{DR} ridge (Figs. 21b and 21c). The low ρ_{hv} pockets denoting the location of dust/debris are collocated with the northeastern section of the gust front convergence zone unlike at the previous time (Fig. 21a). The inner band of convergence still encircles the high-reflectivity ring associated with the hook echo (Fig. 20b). The band also encompasses the TDS although the northern segment is $\sim 200 \text{ m}$ south of the lofted debris signature (Fig. 21a). The northern region of the TDS outside the band of convergence is likely characterized by very small debris particles owing to the low radar reflectivity. An area of divergence is located within the hook echo and may be associated with an axial downdraft (Fig. 21b).

The regions of lofted dust/debris that were located to the south of the El Reno tornado were examined based on a photogrammetric analysis of the high-resolution video recorded at the RaXPoL site near Banner Road and Interstate 40 (Fig. 1) during the period 2324:52–2324:55 UTC. The updraft and radial inflow could be estimated by tracking these prominent features assuming that the difference between particle motion and the winds were small (i.e., particles were small and associated with low terminal velocities). The outline of one coherent region of dust/debris at four different times was attempted (Fig. 22). Tracking the apex of the region led to estimates of the radial inflow and vertical velocity in the plane of the photo for two time intervals (2324:52–2324:54 and 2324:54–2324:55 UTC) as shown in the figure. The increase in both wind components as the dust/debris pockets approached the funnel is apparent. Errors in estimating the edge of the dust cloud were assessed. These errors could result in a $2\text{--}3 \text{ m s}^{-1}$ uncertainty in the derived velocities. The photogrammetric wind estimates were made near the same time of the dual-Doppler wind field for the second volume (2324:54 UTC). The maximum in vertical vorticity

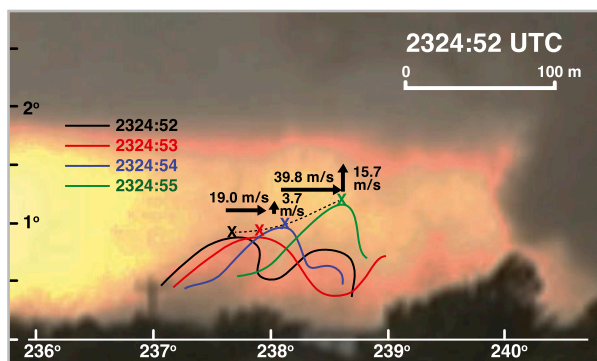


FIG. 22. Photogrammetric analysis of the region south of the El Reno tornado at 2324:52 UTC depicting the progression of dust/debris into the funnel. The observations times are shown by the different colors and are based on a high-definition video. The movement of a ridge of a dust/debris cloud is indicated by the “X.” The black arrows denote the horizontal and vertical velocities in the plane of the photograph calculated by tracking the ridge during the period 2324:52–2324:55 UTC. The video was recorded from the RaXPoL site near Banner Road and Interstate 40 (Fig. 1).

[denoted by the crisscross (“X”)] is located within the WEH (Fig. 23a). The tracking of the lofted dust/debris shown in the previous figure was centered along the 238° azimuth from RaXPoL (Fig. 22). The location of the visual pocket of dust/debris could be located by the intersection of this azimuth with the region of low ρ_{hv} in the radar scan (white dot in Fig. 23). The horizontal projection of the vertical plane of the video image is also plotted in Fig. 23a. The tornado-relative radial inflow based on the dual-Doppler wind synthesis is $\sim 20 \text{ m s}^{-1}$ at the location of the feature identified in the video image. Quantitative comparisons with the results shown in Fig. 22 are difficult since the dual-Doppler winds are spatially filtered and are presented for one height; however, the estimated inflow based on the photogrammetrically tracked dust/debris pocket is consistent with the synthesized winds.

The pockets of dust/debris that produce tail-like features shown in the present study (Figs. 19a, 21a, and 23b) are different than the debris ejection described by Kurdzo et al. (2015) although both produce similar ρ_{hv} signatures. The video of the El Reno tornado did not record debris being ejected into the region occupied by these pockets. Instead, high winds at the leading edge of the rear-flank gust front appeared to be lofting dust/debris particles that were, subsequently, advected toward the tornado (Figs. 20 and 21).

5. Discussion and summary

The El Reno tornado was a large and intense tornado that remained primarily over open terrain and resulted

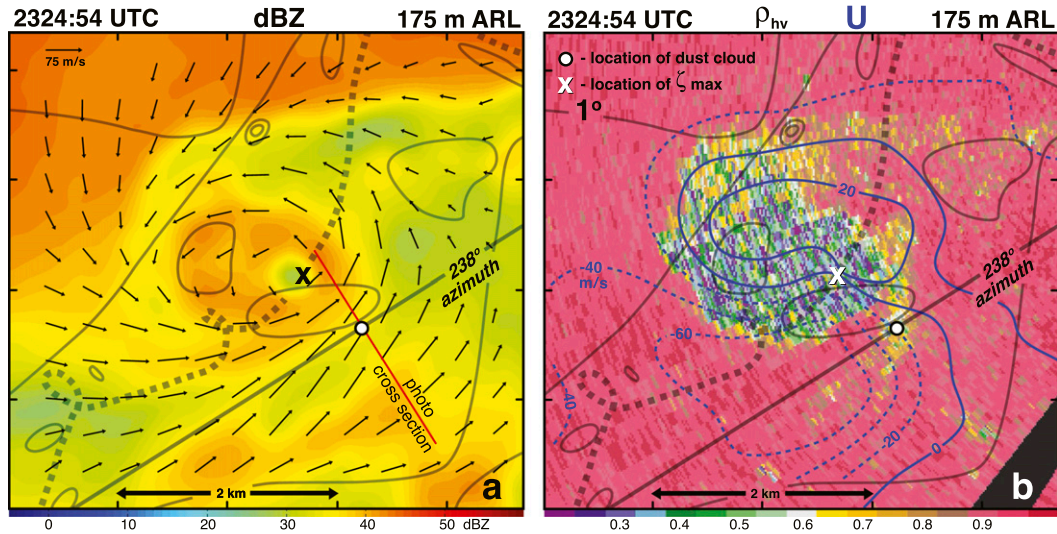


FIG. 23. Dual-Doppler analysis at 2324:54 UTC at 175 m ARL. (a) Radar reflectivity and the ground-relative wind field, and (b) ρ_{hv} superimposed on isopleths of the tornado-relative radial velocity U . Positive and negative U are shown as solid and dashed blue lines, respectively. The 238° azimuth from RaXPol is drawn. The white circle is the location of the dust/debris that was tracked in a movie shown in Fig. 22. The \times is the location of the maximum of vertical vorticity (nearly coincident with the weak-echo eye in radar reflectivity) that denotes the origin for the U calculations. The EF isopleths and center of the tornado track are superimposed as gray lines. The RaXPol scan at 1° elevation angle for ρ_{hv} is shown in (b).

in the deaths of several storm chasers. The current study presented a detailed analysis of the damage survey of the tornado track combined with data recorded by two rapidly scanning radars. The relationship between several suction vortices visually identified in pictures with the high-resolution radar data and swath marks in fields are discussed. The suction vortices were associated with small shear features in Doppler velocity and a partial ringlike feature of high spectral width. Later in the tornado's life cycle, a large number of rotational couplets/shear features were accompanied by a pronounced ring of high spectral width. One large suction vortex in the present study was estimated to be translating at $\sim 76.7 \text{ m s}^{-1}$ [consistent with analysis presented by Snyder and Bluestein (2014) and Wurman et al. (2014)] and was tracked in a movie as it created an arclike damage swath at the surface. This combination of visual documentation of the funnel, Doppler radar analysis of the rotational couplet, and damage swath at the surface of a suction vortex has not been previously attempted.

A dual-Doppler wind synthesis of the circulation at low levels based on data collected by RSDOW and RaXPol for three consecutive times was presented. There was one region associated with wind speeds greater than 90 m s^{-1} at 175 m ARL (maximum grid-point value was 95 m s^{-1}), exceeding the minimum wind speed for EF5 damage. The analysis of the vertical vorticity field appeared to suggest a rapid transition

from a single tornadic vortex centered on the WEH to suction vortices surrounding the WEH and collocated with the ring of enhanced radar reflectivities. The wind synthesis supports earlier single-Doppler observations of this tornado (e.g., Snyder and Bluestein 2014; Wurman et al. 2014). Several bands/zones of enhanced convergence were identified and are summarized in Fig. 24. One of these convergence bands denotes the position of an internal or secondary rear-flank gust front (yellow dashed line). An inner convergence band (gray line), however, may be a result of a positive bias in radial velocity due to centrifuging of large lofted debris swirling within the tornado. An outer convergence band (brown line) is hypothesized to occur at the northern edge of the TDS, which denotes the northern extent of a region of strong inflow into the hook echo. The strong wind speeds in the inflow are progressively lofting small debris and dust as air moves from east to west into weak-echo notch of the hook. To the authors' knowledge, this may be the first time that the positive bias in tornado-relative radial velocities owing to lofted debris has been resolved in a Doppler radar analysis. The schematic model also highlights the Z_{DR} ridge located between the hook echo and rear-flank gust front, which is suspected to comprise larger hydrometeors being advected by the rear-flank outflow. The dust/debris particles to the south of the tornado are also shown in the schematic. The black and magenta flow lines drawn

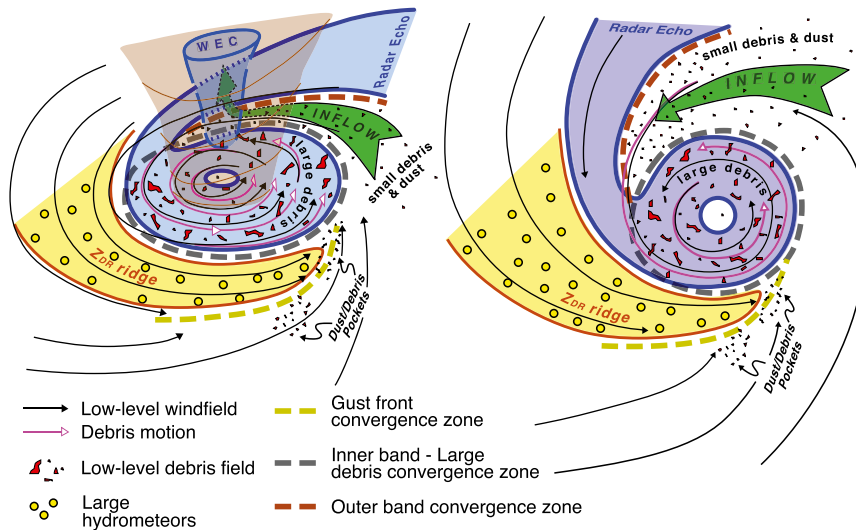


FIG. 24. Three-dimensional and horizontal schematic models that summarize the low-level wind field and its relation to the debris motion for the El Reno tornado. The debris particles within the tornado and dust/debris pockets south of the tornado are illustrated in the figure. Hydrometeors within a Z_{DR} ridge are indicated in the yellow shaded region. The differences between the wind field and debris motion are shown by the black and magenta lines, respectively. Three regions of maximum convergence are indicated by brown, gray, and yellow dashed lines. The thick green arrow denotes inflow into the hook echo that lofts dust and small debris as it approaches the weak-echo notch.

within the hook echo depict the wind field and particle trajectories, respectively, in order to illustrate the impact of centrifuging.

Mobile, rapid-scan radars equipped with polarimetric capability are collecting unusually detailed data on the tornado and surrounding features. The ability to produce high-resolution dual-Doppler wind syntheses in the present study has further elucidated the complex interaction between the winds and the hydrometeors/debris. Combining these analyses with comprehensive aerial/ground surveys and photogrammetric analyses of the visual features of the funnel and debris field have been rare but are needed in order to understand the kinematic structure of tornadoes and how it relates to the damage intensity and patterns identifiable over open terrain and to structures.

Acknowledgments. Research results presented in this paper were supported by the National Science Foundation (NSF) RAPID AGS-1343963 and AGS-1242339 (through NTA), AGS-0934307 and AGS-1262048 (through HBB), and the Independent and Research/Development (IRD) program (through RMW). RSDOW is supported by NSF AGS-1361237 and 1447268. The authors wish to express their appreciation to Don Burgess and Tim Marshall for providing damage survey information that was included in the results shown in this

paper. Comments from two anonymous reviewers substantially improved an earlier version of the manuscript.

REFERENCES

- Atkins, N. T., A. McGee, R. Ducharme, R. M. Wakimoto, and J. Wurman, 2012: The LaGrange tornado during VORTEX2. Part II: Photogrammetric analysis of the tornado combined with dual-Doppler radar data. *Mon. Wea. Rev.*, **140**, 2939–2958, doi:10.1175/MWR-D-11-00285.1.
- , K. M. Butler, K. R. Flynn, and R. M. Wakimoto, 2014: An integrated damage, visual, and radar analysis of the 2013 Moore Oklahoma EF5 tornado. *Bull. Amer. Meteor. Soc.*, **95**, 1549–1561, doi:10.1175/BAMS-D-14-00033.1.
- Barnes, S. L., 1964: A technique for maximizing details in numerical weather map analysis. *J. Appl. Meteor.*, **3**, 396–409, doi:10.1175/1520-0450(1964)003<0396:ATFMDI>2.0.CO;2.
- Bech, J., M. Gaya, M. Aran, F. Figuerola, J. Amaro, and J. Arus, 2009: Tornado damage analysis of a forest area using site survey observations, radar data and a simple analytical vortex model. *Atmos. Res.*, **93**, 118–130, doi:10.1016/j.atmosres.2008.10.016.
- Beck, V., and N. Dotzek, 2010: Reconstruction of near-surface tornado wind fields from forest damage. *J. Appl. Meteor. Climatol.*, **49**, 1517–1537, doi:10.1175/2010JAMC2254.1.
- Bettes, M., 2014: The tornado hunt—Experiences from The Weather Channel. *Major Weather Events and Societal Impacts of 2013*, Atlanta, GA, Amer. Meteor. Soc., 3.3. [Available online at <https://ams.confex.com/ams/94Annual/webprogram/Paper242158.html>.]
- Bluestein, H. B., W. P. Unruh, D. C. Dowell, T. A. Hutchinson, T. M. Crawford, A. C. Wood, and H. Stein, 1997: Doppler

- radar analysis of the Northfield, Texas, tornado of 25 May 1994. *Mon. Wea. Rev.*, **125**, 212–230, doi:10.1175/1520-0493(1997)125<0212:DRAOTN>2.0.CO;2.
- , B. A. Albrecht, R. M. Hardesty, W. D. Rust, D. Parsons, R. Wakimoto, and R. M. Rauber, 2001: Ground-based mobile instrument workshop summary, 23–24 February 2000, Boulder, Colorado. *Bull. Amer. Meteor. Soc.*, **82**, 681–694, doi:10.1175/1520-0477(2001)082<0681:MSGMIW>2.3.CO;2.
- , M. M. French, R. L. Tanamachi, S. Frasier, K. Hardwick, F. Junyent, and A. L. Pazmany, 2007: Close-range observations of tornadoes in supercells made with a dual-polarization, X-band, mobile Doppler radar. *Mon. Wea. Rev.*, **135**, 1522–1543, doi:10.1175/MWR3349.1.
- , J. C. Snyder, and J. B. Houser, 2015: A multiscale overview of the El Reno, Oklahoma, tornadic supercell of 31 May 2013. *Wea. Forecasting*, **30**, 525–552, doi:10.1175/WAF-D-14-00152.1.
- , M. M. French, J. C. Snyder, and J. B. Houser, 2016: Doppler radar observations of anticyclonic tornadoes in cyclonically rotating, right-moving supercells. *Mon. Wea. Rev.*, doi:10.1175/MWR-D-15-0304.1, in press.
- Bodine, D. J., M. R. Kumjian, R. D. Palmer, P. L. Heinselman, and A. V. Ryzhkov, 2013: Tornado damage estimation using polarimetric radar. *Wea. Forecasting*, **28**, 139–158, doi:10.1175/WAF-D-11-00158.1.
- Browning, K. A., 1964: Airflow and precipitation trajectories within severe local storms which travel to the right of the winds. *J. Atmos. Sci.*, **21**, 634–639, doi:10.1175/1520-0469(1964)021<0634:AAPTWS>2.0.CO;2.
- Burgess, D. W., M. A. Magsig, J. Wurman, D. C. Dowell, and Y. Richardson, 2002: Radar observations of the 3 May 1999 Oklahoma City tornado. *Wea. Forecasting*, **17**, 456–471, doi:10.1175/1520-0434(2002)017<0456:ROOTMO>2.0.CO;2.
- Doswell, C. A., III, and D. W. Burgess, 1988: On some issues of United States tornado climatology. *Mon. Wea. Rev.*, **116**, 495–501, doi:10.1175/1520-0493(1988)116<0495:OSIOUS>2.0.CO;2.
- , H. E. Brooks, and N. Dotzek, 2009: On the implementation of the enhanced Fujita scale in the USA. *Atmos. Res.*, **93**, 554–563, doi:10.1016/j.atmosres.2008.11.003.
- Dowell, D. C., C. R. Alexander, J. M. Wurman, and L. J. Wicker, 2005: Centrifuging of hydrometeors and debris in tornadoes: Radar reflectivity patterns and wind measurement errors. *Mon. Wea. Rev.*, **133**, 1501–1524, doi:10.1175/MWR2934.1.
- Edwards, R., J. G. LaDue, J. T. Ferree, K. Scharfenberg, C. Maier, and W. L. Coulbourne, 2013: Tornado intensity estimation. *Bull. Amer. Meteor. Soc.*, **94**, 641–653, doi:10.1175/BAMS-D-11-00006.1.
- French, M. M., D. W. Burgess, E. R. Marshall, and L. J. Wicker, 2015: Bulk hook echo raindrop sizes retrieved using mobile, polarimetric Doppler radar observations. *J. Appl. Meteor. Climatol.*, **54**, 423–450, doi:10.1175/JAMC-D-14-0171.1.
- Fujita, T. T., 1981: Tornadoes and downbursts in the context of generalized planetary scales. *J. Atmos. Sci.*, **38**, 1511–1534, doi:10.1175/1520-0469(1981)038<1511:TADITC>2.0.CO;2.
- , 1989: The Teton-Yellowstone tornado of 21 July 1987. *Mon. Wea. Rev.*, **117**, 1913–1940, doi:10.1175/1520-0493(1989)117<1913:TTYTOJ>2.0.CO;2.
- , 1992: *Memoirs of an Effort to Unlock Mystery of Severe Storms during the 50 Years, 1942-1992*. University of Chicago Press, 298 pp.
- , D. L. Bradbury, and C. F. Van Thullenar, 1970: Palm Sunday tornadoes of April 1, 1965. *Mon. Wea. Rev.*, **98**, 29–69, doi:10.1175/1520-0493(1970)098<0029:PSTOA>2.3.CO;2.
- , G. S. Forbes, and T. A. Umenhofer, 1976: Close-up view of 20 March 1976 tornadoes: Sinking cloud tops to suction vortices. *Weatherwise*, **29**, 116–145, doi:10.1080/00431672.1976.10544142.
- Fujiwhara, S., 1931: Short note on the behavior of two vortices. *Proc. Math. Soc. Japan*, **13**, 106–110.
- Golden, J. H., and D. Purcell, 1978: The life cycle of the Union City, Oklahoma tornado and comparisons with waterspouts. *Mon. Wea. Rev.*, **106**, 3–11, doi:10.1175/1520-0493(1978)106<0003:LCOTUC>2.0.CO;2.
- Hildebrand, P. H., and R. K. Moore, 1990: Meteorological radar observations from mobile platforms. *Radar in Meteorology*, D. Atlas, Ed., Amer. Meteor. Soc., 287–314.
- Houser, J. B., H. B. Bluestein, and J. C. Snyder, 2015: Rapid-scan, polarimetric, Doppler radar observations of tornadogenesis and tornado dissipation in a tornadic supercell: The “El Reno, Oklahoma” storm of 24 May 2011. *Mon. Wea. Rev.*, **143**, 2685–2710, doi:10.1175/MWR-D-14-00253.1.
- Karstens, C. D., T. M. Samaras, B. D. Lee, W. A. Gallus, and C. A. Finley, 2010: Near-ground pressure and wind measurements in tornadoes. *Mon. Wea. Rev.*, **138**, 2570–2588, doi:10.1175/2010MWR3201.1.
- , W. A. Gallus, B. D. Lee, and C. A. Finley, 2013: Analysis of tornado-induced tree fall using aerial photography from the Joplin, Missouri, and Tuscaloosa–Birmingham, Alabama, tornadoes of 2011. *J. Appl. Meteor. Climatol.*, **52**, 1049–1068, doi:10.1175/JAMC-D-12-0206.1.
- Keeler, R. J., and R. E. Passarelli, 1990: Signal processing for atmospheric radars. *Radar in Meteorology*, D. Atlas, Ed., Amer. Meteor. Soc., 199–229.
- Kosiba, K. A., and J. Wurman, 2013: The three-dimensional structure and evolution of a tornado boundary layer. *Wea. Forecasting*, **28**, 1552–1561, doi:10.1175/WAF-D-13-00070.1.
- Kumjian, M. R., 2011: Precipitation properties of supercell hook echoes. *Electron. J. Severe Storms Meteor.*, **6**, 1–21.
- , and A. V. Ryzhkov, 2008: Polarimetric signatures in supercell thunderstorms. *J. Appl. Meteor. Climatol.*, **47**, 1940–1961, doi:10.1175/2007JAMC1874.1.
- Kurdzo, J. M., D. J. Bodine, B. L. Cheong, and R. D. Palmer, 2015: High-temporal resolution polarimetric X-band Doppler radar observations of the 20 May 2013 Moore, Oklahoma. *Mon. Wea. Rev.*, **143**, 2711–2735, doi:10.1175/MWR-D-14-00357.1.
- LaDue, J. G., and E. A. Mahoney, 2006: Implementing the new enhanced Fujita scale within the NWS. *23rd Conf. on Severe Local Storms*, St. Louis, MO, Amer. Meteor. Soc., 5.5. [Available online at https://ams.confex.com/ams/23SLS/techprogram/paper_115420.htm.]
- Lee, B. D., C. A. Finley, and C. D. Karstens, 2012: The Bowdle, South Dakota, cyclic tornadic supercell of 22 May 2010: Surface analysis of rear-flank downdraft evolution and multiple internal surges. *Mon. Wea. Rev.*, **140**, 3419–3441, doi:10.1175/MWR-D-11-00351.1.
- Lee, W.-C., and J. Wurman, 2005: Diagnosed three-dimensional axisymmetric structure of the Mulhall tornado on 3 May 1999. *J. Atmos. Sci.*, **62**, 2373–2393, doi:10.1175/JAS3489.1.
- Lemon, L. R., and C. A. Doswell III, 1979: Severe thunderstorm evolution and mesocyclone structure as related to tornadogenesis. *Mon. Wea. Rev.*, **107**, 1184–1197, doi:10.1175/1520-0493(1979)107<1184:STEAMS>2.0.CO;2.
- Majcen, M., P. Markowski, Y. Richardson, D. Dowell, and J. Wurman, 2008: Multipass objective analyses of Doppler radar data. *J. Atmos. Oceanic Technol.*, **25**, 1845–1858, doi:10.1175/2008JTECHA1089.1.

- Marquis, J., Y. Richardson, J. Wurman, and P. M. Markowski, 2008: Single- and dual-Doppler analysis of a tornadic vortex and surrounding storm-scale flow in the Crowell, Texas, supercell of 30 April 2000. *Mon. Wea. Rev.*, **136**, 5017–5043, doi:10.1175/2008MWR2442.1.
- Marshall, T. P., 2002: Tornado damage at Moore, Oklahoma. *Wea. Forecasting*, **17**, 582–598, doi:10.1175/1520-0434(2002)017<0582:TDSAMO>2.0.CO;2.
- , D. Burgess, G. Garfield, R. Smith, D. Speheger, J. Snyder, and H. Bluestein, 2014: Ground-based damage survey and radar analysis of the El Reno, Oklahoma tornado. *27th Conf. on Severe Local Storms*, Madison, WI, Amer. Meteor. Soc., 13.1. [Available online at <https://ams.confex.com/ams/27SLS/webprogram/Paper254342.html>.]
- Nolan, D. S., 2013: On the use of Doppler radar-derived wind fields to diagnose the secondary circulations of tornadoes. *J. Atmos. Sci.*, **70**, 1160–1171, doi:10.1175/JAS-D-12-0200.1.
- Palmer, R. D., and Coauthors, 2011: Observations of the 10 May 2010 tornado outbreak using OU-PRIME: Potential for new science with high-resolution polarimetric radar. *Bull. Amer. Meteor. Soc.*, **92**, 871–891, doi:10.1175/2011BAMS3125.1.
- Pauley, P. M., and X. Wu, 1990: The theoretical, discrete, and actual response of the Barnes objective analysis scheme for one- and two-dimensional fields. *Mon. Wea. Rev.*, **118**, 1145–1163, doi:10.1175/1520-0493(1990)118<1145:TTDAAR>2.0.CO;2.
- Pazmany, A. L., J. B. Mead, H. B. Bluestein, J. C. Snyder, and J. B. Houser, 2013: A mobile rapid-scanning X-band polarimetric (RaXPo) Doppler radar system. *J. Atmos. Oceanic Technol.*, **30**, 1398–1413, doi:10.1175/JTECH-D-12-00166.1.
- Snyder, J. C., and H. B. Bluestein, 2014: Some considerations for the use of high-resolution mobile radar data in tornado intensity determination. *Wea. Forecasting*, **29**, 799–827, doi:10.1175/WAF-D-14-00026.1.
- Tanamachi, R. L., H. B. Bluestein, J. B. Houser, S. J. Frasier, and K. M. Hardwick, 2012: Mobile, X-band, polarimetric Doppler radar observations of the 4 May 2007 Greensburg, Kansas tornadic supercell. *Mon. Wea. Rev.*, **140**, 2103–2125, doi:10.1175/MWR-D-11-00142.1.
- Wakimoto, R. M., H. V. Murphey, D. C. Dowell, and H. B. Bluestein, 2003: The Kellerville tornado during VORTEX: Damage survey and Doppler radar analyses. *Mon. Wea. Rev.*, **131**, 2197–2221, doi:10.1175/1520-0493(2003)131<2197:TKTDVD>2.0.CO;2.
- , N. T. Atkins, and J. Wurman, 2011: The LaGrange tornado during VORTEX2. Part I: Photogrammetric analysis of the tornado combined with single-Doppler radar data. *Mon. Wea. Rev.*, **139**, 2233–2258, doi:10.1175/2010MWR3568.1.
- , P. Stauffer, W.-C. Lee, N. T. Atkins, and J. Wurman, 2012: Finescale structure of the LaGrange, Wyoming, tornado during VORTEX2: GBVTD and photogrammetric analyses. *Mon. Wea. Rev.*, **140**, 3397–3418, doi:10.1175/MWR-D-12-00036.1.
- , N. T. Atkins, K. M. Butler, H. B. Bluestein, K. Thiem, J. Snyder, and J. Houser, 2015: Photogrammetric analysis of the El Reno tornado combined with mobile X-band polarimetric radar data. *Mon. Wea. Rev.*, **143**, 2657–2683, doi:10.1175/MWR-D-15-0034.1.
- Wurman, J., 2002: The multiple-vortex structure of a tornado. *Wea. Forecasting*, **17**, 473–505, doi:10.1175/1520-0434(2002)017<0473:TMVSOA>2.0.CO;2.
- , and S. Gill, 2000: Finescale radar observations of the Dimmitt, Texas (2 June 1995) tornado. *Mon. Wea. Rev.*, **128**, 2135–2164, doi:10.1175/1520-0493(2000)128<2135:FROOTD>2.0.CO;2.
- , and M. Randall, 2001: An inexpensive, mobile, rapid-scan radar. Preprints, *30th Int. Conf. on Radar Meteorology*, Munich, Germany, Amer. Meteor. Soc., P3.4. [Available online at https://ams.confex.com/ams/30radar/techprogram/paper_21577.htm.]
- , and C. R. Alexander, 2005: The 30 May 1998 Spencer, South Dakota, storm. Part II: Comparison of observed damage and radar-derived winds in the tornadoes. *Mon. Wea. Rev.*, **133**, 97–119, doi:10.1175/MWR-2856.1.
- , and K. Kosiba, 2013: Finescale radar observations of tornado and mesocyclone structures. *Wea. Forecasting*, **28**, 1157–1174, doi:10.1175/WAF-D-12-00127.1.
- , Y. Richardson, C. Alexander, S. Weygandt, and P. F. Zhang, 2007: Dual-Doppler and single-Doppler analysis of a tornadic storm undergoing mergers and repeated tornadogenesis. *Mon. Wea. Rev.*, **135**, 736–758, doi:10.1175/MWR3276.1.
- , K. Kosiba, and P. Robinson, 2013: In situ, Doppler radar, and video observations of the interior structure of a tornado and the wind-damage relationship. *Bull. Amer. Meteor. Soc.*, **94**, 835–846, doi:10.1175/BAMS-D-12-00114.1.
- , —, —, and T. Marshall, 2014: The role of multiple-vortex tornado structure in causing storm researcher fatalities. *Bull. Amer. Meteor. Soc.*, **95**, 31–45, doi:10.1175/BAMS-D-13-00221.1.